Journal of
Manufacturing and Materials Processing

MDPI

Article

Small- to Large-Scale Electron Beam Powder Bed Fusion of Functionally Graded Steels

Carlos Botero [1], William Sjöström [1,*], Emilio Jimenez-Pique [2], Andrey Koptyug [1] and Lars-Erik Rännar [1]

[1] Sports Tech Research Centre, Mid Sweden University, Akademigatan 1, SE-83140 Östersund, Sweden; carlos.botero@miun.se (C.B.); andrey.koptyug@miun.se (A.K.); lars-erik.rannar@miun.se (L.-E.R.)
[2] Barcelona Research Center in Multiscale Science and Engineering, Universitat Politècnica de Catalunya, Campus Diagonal Besòs—EEBE, 08019 Barcelona, Spain; emilio.jimenez@upc.edu
* Correspondence: william.sjostrom@miun.se

Abstract: The ability to control process parameters over time and build space in electron beam powder bed fusion (PBF-EB) opens up unprecedented opportunities to tailor the process and use materials of a different nature in the same build. The present investigation explored the various methods used to adapt the PBF-EB process for the production of functionally graded materials (FGMs). In this way, two pre-alloyed powders—a stainless steel (SS) powder and a highly alloyed cold work tool steel (TS) powder—were combined during processing in an S20 Arcam machine. Feasibility experiments were first carried out in a downscaled build setup, in which a single powder container was installed on top of the rake system. In the container, one powder was placed on top of the other (SS/TS) so that the gradient materials were produced as the powders were spread and intermixed during the build. The process was later scaled up to an industrial machine setup, where a similar approach was implemented using two configurations of powder disposal: SS/SS + TS/TS and TS/TS + SS/SS. Each configuration had an intermediate layer of powder blend. The FGMs obtained were characterized in terms of their microstructure and local and macromechanical properties. For the microstructural analysis, optical microscopy, scanning electron microscopy (SEM), and energy-dispersive X-ray spectroscopy (EDX) were performed on the polished cross-sections. This provided evidence of gradual microstructural and compositional transitions in the samples, with a shift from SS to TS and vice versa. Nanoindentation experiments confirmed that there was a consequent gradient in the hardness, stiffness, and wear ratio from the softer and ductile SS to the harder and stiff TS. Scratch experiments revealed gradual evolution in the sliding wear behavior of the printed materials. A "progressive spring" and a "hardness-tailored punching tool" were fabricated as demonstrators. The results obtained demonstrate the great potential to gradually tailor the composition, microstructure, mechanical properties, and wear resistance by combining different powders, and they suggest that any PBF-EB system can be repurposed to build gradient materials without hardware modification. Potential applications include the tooling industry, where hard and wear-resistant materials are needed for the surfaces of tools, with tougher and more ductile materials used in the cores of tools.

Keywords: electron beam powder bed fusion; multi-materials; tool steel; stainless steel

Academic Editors: Elham Mirkoohi and Hamed Asgari

Received: 21 November 2024
Revised: 16 December 2024
Accepted: 19 December 2024
Published: 29 December 2024

Citation: Botero, C.; Sjöström, W.; Jimenez-Pique, E.; Koptyug, A.; Rännar, L.-E. Small- to Large-Scale Electron Beam Powder Bed Fusion of Functionally Graded Steels. *J. Manuf. Mater. Process.* **2025**, *9*, 7. https://doi.org/10.3390/jmmp9010007

1. Introduction

Electron beam powder bed fusion (PBF-EB) is one of the fastest-growing additive manufacturing (AM) technologies available for the manufacturing of metals. In PBF-EB, components are built up layer by layer via the action of an electron beam in a process

that takes place under vacuum conditions (partial helium pressure of 2×10^{-3} mbar) at high temperatures (typically between ~700 and 1100°C). Each layer is completed with a pre-sintering stage, in which a defocused beam is used to preheat the powder, followed by a melting stage, in which a focused beam is used for powder consolidation. Most typical examples of PBF-EB use pre-alloyed powders such as Ti-6Al-4V [1] and TiAl [2], Ni-based alloys (IN625 [3], IN718 [4,5], and Alloy 247 [6]), and Co-Cr-Mo [7].

In recent years, both industry and academia have shown increasing interest in the development of the PBF-EB process for iron-based and steel materials. Some successful examples include stainless steels, such as 316L [8–11] and super duplex steels [12], as well as highly alloyed cold work tool steels [13,14]. The ability of PBF-EB to steer the beam-related process parameters permits control over the localized melt pool characteristics and the solidification behavior. This, together with the protective vacuum environment and the possibility to control the build temperature, opens up great possibilities for the tailoring and adaptation of the process for the use of powders of a different nature during the same build [15,16]. Despite this potential, efforts to combine different powders in PBF-EB technology have been somewhat limited because the commercially available machines are designed for the processing of a powder of one specific alloy during the build process.

Many applications would benefit from the possibility of one-step manufacturing processes that allow the use of multi-material metallic components with complex geometries. Traditional joining processes, such as welding, face several challenges, including concerns related to the compatibility of dissimilar materials, the buildup of residual stresses, the formation of intermetallic phases and non-melted particles, the complexity of the geometry, etc. [17]. In this context, AM processes are being increasingly explored as an alternative to overcome such challenges in the fabrication of FGMs [17–20], where the spatial variation in composition across the volume allows for the corresponding tailoring of the material properties to meet functional requirements.

Two machine hardware setups were used in combination with different powder disposal configurations to achieve in situ gradual powder mixing during the build process. The process was set up to enable parameter adjustment for the pre-heating and melting of the two powders, yielding dense specimens with no signs of cracking. The experiments were based on the authors' previous experience in material and process development for PBF-EB in general and iron-based materials in particular [8–16,21,22]. The proposed approach proved to be successful in gradually tailoring the microstructure, composition, and mechanical properties of the manufactured specimens, from the softer and ductile ones of a stainless steel to the harder and stiffer ones of a tool steel. A "progressive spring" and a "hardness-tailored punching tool" were manufactured as demonstrators to validate the functional gradient variations in stiffness and hardness, respectively. The results obtained suggest that almost any PBF-EB system can be reset to produce gradient materials without hardware modification. This opens up great possibilities for a wide range of applications, such as in the tooling industry, where hard and wear-resistant materials are needed for tool surfaces, while tougher and more ductile materials are used in the cores of tools.

2. PBF of Multi-Materials: State of the Art

Various metal AM techniques have been explored for the fabrication of multi-materials. Due to its ability to easily feed multiple powder streams or wire types, direct energy deposition (DED) has been used to combine powders of a dissimilar nature during processing [23]. Elemental and pre-alloyed powders have been combined in various ways to achieve in situ alloying [23–26] and to manufacture composite materials [23], multi-layered materials [23,27,28], and FGMs [17,18,23,28–31]. The high accuracy and design freedom of PBF methods, as well as the fact that they represent the majority of the global metal AM market,

has motivated increasing interest in the further development of both laser (PBF-LB) and electron beam (PBF-EB) technologies for multi-material processing. Similar efforts to combine dissimilar powders have also been reported for PBF methods. In PBF-LB, for instance, blends of elemental powders such as Ti, Ni [32] and Al, Si [33] were used as precursors, aiming to explore in situ alloying, and metal–ceramic blends such as WC, Co [34] were implemented in the manufacturing of composite materials. In the case of PBF-EB technologies, the blending of powders has also been explored to enable in situ alloying using pre-alloyed and elemental powder blends such as Mn, Al [35]; Al, Cr, Mo, Nb, Ta [36]; Ni, Ti [26]; In718, CoCr75 [20,21]; Ti6Al4V, Ti45Al7Nb [37]; and Ti, Nb [38]. Metal–ceramic powder combinations such as 316L, WC [15] and Ti6Al4V and hydroxyapatite [39] have also been implemented to obtain composite materials. In the case of steels, it has even been reported that the pre-blending of two iron-based powders, 316L and Colferoloy, in combination with the steering of the electron beam process parameters, allows one to engineer the composition and microstructure of the resulting materials so that it is possible to achieve composite-like and in situ alloying in selected areas within the same component [16].

Different strategies have been implemented to achieve FGMs by combining dissimilar powders as feedstocks using PBF-LB methods. Multi-directional compositional gradients have been attempted by installing various adaptable multi-powder dispensing systems, in which the deposition of different materials can be locally controlled in synchrony with adapted process parameters for each material composition. This approach has been shown to be effective in achieving material gradients in both the horizontal (XY, perpendicular to the build axis) and vertical directions (Z, parallel to the build axis). Some examples of materials with gradual transitions in the horizontal direction, obtained using PBF-LB, are Ti-xTa [40], 316L-CuCrZr [20], 1.2709-CuCrZr [41], 316L-In718-Cu10Sn [42], CoCrMo-In718 [43], and 316L-In718 [32]. Furthermore, the company Aerosint (Herstal, Belgium) recently presented selective powder deposition (SPD) technology, a setup based on rotating drums that can be integrated into PBF-LB systems, allowing for the selective deposition of multiple powders, forming a single layer containing at least two materials [44].

Several approaches have also been reported for materials with gradients in the build direction. A multi-material unit installed in a PBF-LB system was used to blend Ti6Al4V and IN718 powders during the build process to achieve vertical, compositionally graded materials [45]. The results of this investigation show that different proportions of materials in the powder blend lead to quite different microstructures and gradients in the composition and hardness, depending on the degree of in situ alloying and the presence of hard inclusions. The graded processing in PBF-LB systems has been shown to pose challenges due to both the low compatibility of the alloying elements and the high thermal gradients, leading to cracking for some composition–parameter combinations. In another investigation, 316L SS and IN 718 powders were placed in two hoppers at the sides of the build table in a PBF-LB machine, and discrete layered materials were obtained by alternate powder deposition and melting [46]. Significant Fe and Ni diffusion and dilution were observed in the interfacial zone across three to four layers (30 µm layer thickness). The continuous interface and the gradient hardness profile suggested good metallurgical bonding in the obtained materials. Another strategy, also explored in a PBF-LB machine, implemented a central separator in the powder delivery system to supply 316L SS and C18400 copper alloy to achieve bi-metallic laminates [47]. Although some isolated cracks were observed in the steel side at the interphase, a good metallurgical bond with a continuous microstructure and hardness was evidenced. Spherical steel particles embedded in the copper matrix were also observed in the interphase. Two iron-based materials, 316L SS and MS1 maraging steel, were also used to produce multi-materials with discrete and continuous interfaces in another PBF-LB system [48]. Multiple hoppers were coupled to a rotating screw for selec-

tive powder feeding by extrusion. The materials showed discrete and gradual transitions in their microstructure, composition, and hardness across the interphase.

Very few examples can be found in the open literature of the manufacturing of FGMs by PBF-EB. One-dimensional FGMs of (α_2 + γ) TiAl alloy/(α + β) titanium alloy were achieved from a single material powder by evaporating the alloying elements and altering the beam energy deposition [49]. A PBF-EB system with the capacity for dual-material processing was also reported in [50]. In this system, a powder supplying method based on vibration was used to process Ti-6Al-4V and Ti-47Al-2Cr-2Nb powders and to achieve dual metal structures of Ti-3Al/TiAl and Ti-6Al-4V/Ti-3Al. Functionally graded Cu-W composite materials were also achieved via PBF-EB using a powder blend composed of elemental Cu and W powders with different levels of particle size by implementing a selective raking approach in which the layer thickness was varied during the build process [51].

Within the context of the ideas mentioned above, although there are several attempts to fully explore the possibilities for the processing of multi-materials and specifically FGMs in PBF technologies, especially for PBF-LB systems, there is a lack of research on the possibilities for a simple approach to obtain gradient steel-based materials in the build direction using PBF-EB. By using different configurations in the dispersion of powders, FGMs are achieved by gradually mixing the powders during processing, resulting in components in which the material features, such as the microstructure, composition, and mechanical properties, are gradually changed from an SS to a TS and vice versa.

3. Experimental Section

3.1. Powders

The feedstocks used for the manufacturing experiments were two gas-atomized powders: a stainless steel, hereafter referred to as "SS", and a tool steel, hereafter referred to as "TS". The SS feedstock was a grade 316LN powder (Carpenter, Torshälla, Sweden) with a particle size distribution of 53–150 µm. The nominal chemical composition of the powder material is shown in Table 1. The SEM micrographs in Figure 1a,c show some of the details of the powder morphology and texture. The powder grains were near-spherical with attached satellites. The flowability of the powders was measured using a Hall flowmeter (ASTM B213), yielding ~20 s/50 g. The apparent density was measured according to ASTM B212, yielding values of ~4.89 g/cm^3. The powder batch used for the experiments was recycled several times prior to this investigation.

Table 1. Nominal chemical compositions of SS and TS powders.

	Elemental Composition [wt%]							
	Fe	**Cr**	**Ni**	**Mo**	**Mn**	**Si**	**C**	**V**
316LN	Balance	16–18	12–14	2–3	1.4	0.7	0.03	-
V4E	Balance	4.7	-	3.4	0.4	0.4	1.4	3.7

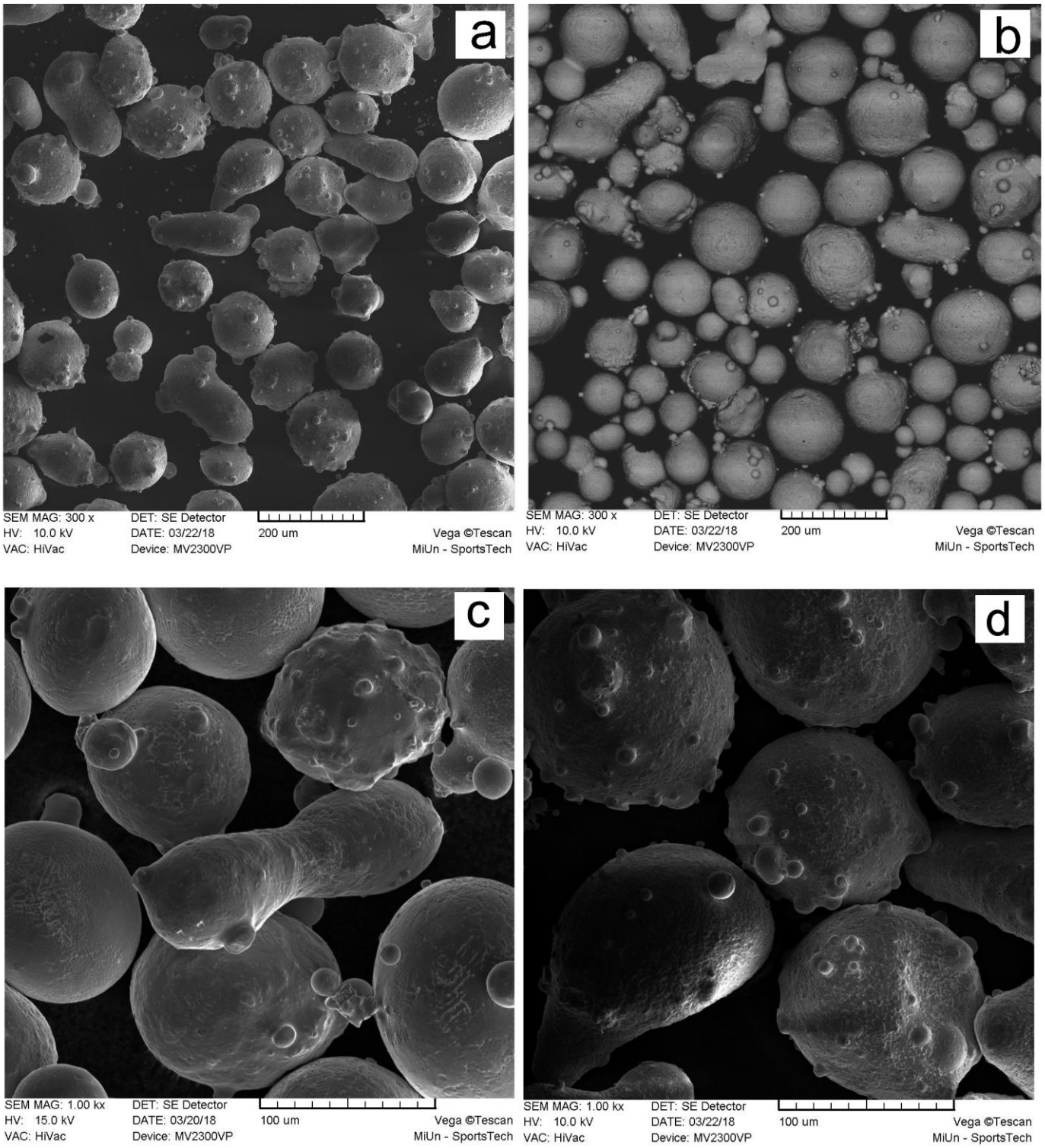

Figure 1. SEM micrographs of the feedstock SS (**a**,**c**) and TS (**b**,**d**) powders at low and high magnification.

The used TS feedstock was a highly alloyed cold work tool steel powder (Vanadis 4 Extra—V4E, Uddeholms AB, Uddeholm, Sweden) with a particle size distribution of 50–150 µm. As can be observed from Table 1, besides carbon (C), the TS had high content of vanadium (V) and molybdenum (Mo), which tend to form carbides, increasing the hardness and strength of this alloy [13,14,52]. The particle size distribution and shape measured according to ISO13322-2 were D10: 51.6 µm, D50: 72.9 µm, and D90: 125.0 µm. The apparent density as measured according to ASTM 212 was 4.42 g/cm^3. Figure 1b,d present

typical SEM images of the TS powder. In contrast to the SS powder, a higher number of satellites is evident on the particles' surface. The flowability, as measured according to ASTM B213, was ~30 s/50 g. This value was slightly higher than that of the SS, which could be attributed to the shape and texture of the TS powder. It was also clear that both powders had mainly near-spherical powder grains, with a few oddly shaped ones, mainly resulting from the merging of a few solidifying droplets of the material. Despite the more irregular particles and rougher surface, the distribution of the TS powder during raking, as well as its spreadability, was acceptable for processing. As with the SS powder, the TS powder was also recycled prior to this investigation.

3.2. Process and Machine Setup

An Arcam S20 EBM system (GE Additive, Mölndal, Sweden) was used for the manufacturing experiments. This system had a 3 KW electron beam gun operating at a 60 kV acceleration voltage. All samples were manufactured using a layer thickness of 50 µm with a snake (raster) scan pattern, with only the hatch theme activated for the melting (no contours). The temperature during the build process was kept at approximately 850 °C by adjusting the beam current and repetition numbers during the pre- and post-heating stages of the builds.

The present investigation aimed to produce an FGM in the PBF-EB system by successively feeding two different steel powders (SS and TS) during the building process. One powder was carefully placed on top of the other in the feeding container. Such powder placement results in three-stage powder feeding: powder one only; a gradual transition from powder one towards powder two; and powder two only. In this way, the first few layers of the print are initially built from the powder placed in the bottom of the container. As the build progresses and the powders continue to flow down to the build table by gravity, a certain amount of powder mixing results in a gradual shift in the material of the printed part towards the second powder placed at the top of the container. Two build setups, depending on which material emerged first, were implemented, as introduced in Sections 3.2.1 and 3.2.2 and illustrated in Figure 2. The authors' experience with the development of the PBF-EB process for the specific materials under investigation (SS and TS) [8–11,13,14] was used to find overlapping regions in their parameter windows, allowing for a stable process yielding continuous solid specimens without changing the parameter settings throughout the manufacturing process.

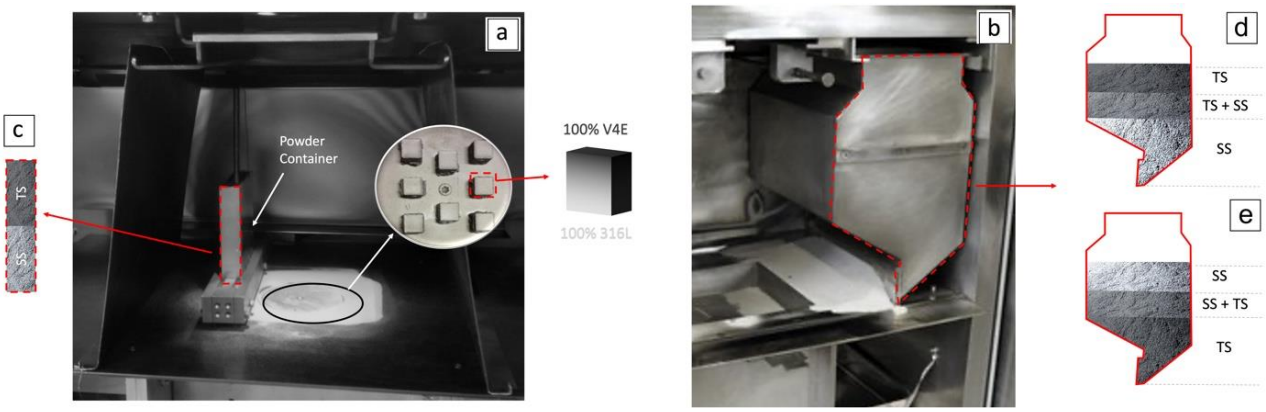

Figure 2. Schematics of the two build setups used for the manufacturing of FGMs: downscaled single hopper setup (**a**) and standard setup (**b**). Different configurations of powder deposition: "*configuration I*" with direct powder transition from SS to TS in the downscaled setup (**c**); "*configuration II*" with gradual powder transition from SS to TS and an intermediate blend of powders (**d**); and "*configuration III*", with gradual powder transition from TS to SS and an intermediate blend of powders (**e**).

3.2.1. Single Hopper Experiments with a Downscaled Setup

In an initial feasibility phase, a scaled-down setup of the machine hardware was used. The modified setup consisted of a cylindrical build table with a 90-mm-diameter build envelope and a rectangular powder feeding system where the container was mounted on top of the rake, feeding the powder between two parallel rake blades, as shown in Figure 2a. More details regarding the implementation of this setup can be found in reference [15].

As illustrated in Figure 2c, the bottom half of the rectangular container (~150 cm^3) was first filled with SS powder, and the top half was later filled with TS powder. In this configuration, hereafter referred to as "*configuration I*", the TS powder flows down first and is spread on the powder bed as the rake moves over the build platform. As the build advances, a transition in the powder dispensing to the table from the SS to the TS occurs after several layers. During this transition, the powders are intermixed, resulting in a gradual evolution from an SS-rich material at the bottom to a TS-rich material on the top of the printed parts.

3.2.2. Single Hopper Operation in Standard Setup

A similar procedure as described in Section 3.2.1 for the downscaled setup was replicated for the standard setup. Two configurations were implemented: "*configuration II*", where the SS powder was placed at the bottom and TS at the top of the container, as presented in Figure 2d, and "*configuration III*", where the TS powder was placed at the bottom and SS at the top, as presented in Figure 2e. In the case of the standard setup, an intermedium layer of a SS + TS powder blend was added in between the individual powders to tailor the gradual transition to a larger region in the final parts. The specific details concerning the volume of the powders available during disposal in the different configurations are summarized in Table 2.

Table 2. Volume of powder used in the different configurations for powder disposal (see Figure 2c,d,e). * Powder blend was 50%SS–50%TS in volume and was prepared by manual mechanical agitation.

Powder	Volume (L)		
	Configuration I	**Configuration II**	**Configuration III**
SS	0.15	2	4.5
SS + TS *	-	0.7	3.5
TS	0.15	4	1

3.2.3. Build Jobs

Three build jobs were compiled to obtain gradient materials, following *configuration I*, *configuration II*, and *configuration III*, as shown in the CAD models presented in Figure 3a,b,c, respectively.

In the initial feasibility study using the downscaled setup and *configuration I*, cubes of 10 × 10 × 5 mm were manufactured on a circular SS start plate, as illustrated in Figure 2a, for the initial trial (8 cubes), and in the CAD model for the manufacturing of the test samples (9 cubes) in Figure 3a. A representative specimen from the test build was further characterized and is referred to as the "*cube*" sample.

A standard 150 × 150 mm SS start plate was used in the standard setup for the build jobs corresponding to *configuration II* and *configuration III* (Figure 3b,c). For *configuration II*, the build included different springs and solid blocks (maximum height z = 60 mm). The samples "*block*" and "*spring*" (see Figure 3b) were selected for characterization. In the case of *configuration III*, besides solid blocks and springs, the build job contained different drilling tools and a metal-forming punch (maximum height z = 80 mm). The sample "punch" (see Figure 3c) was used for further characterization.

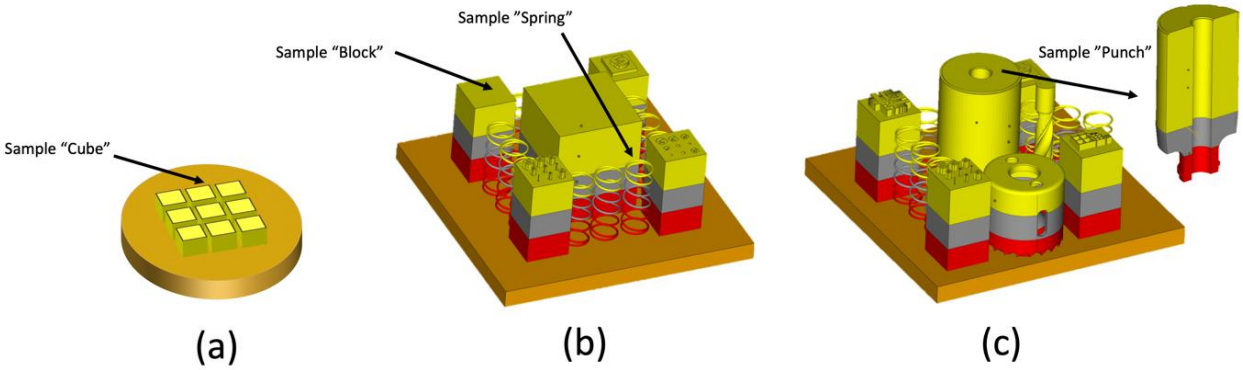

Figure 3. CAD models of the build jobs to obtain gradient materials: 9 cubes in an 82 mm circular-section start plate using *configuration I* (**a**); blocks and springs built in a 150 mm squared start plate using *configuration II* (**b**); blocks, springs, and metal-forming tools (punch and drills) built in a 150 mm squared start plate using *configuration III* (**c**). The different colors in (**b**,**c**) correspond to "segments" created in the build files to account for eventual changes in the parameters needed under processing as the alloying elements change.

3.3. Sample Characterization Methods

To reveal the gradual changes in the functionally graded specimens, the selected specimens presented in Section 3.2.3 were sectioned, encapsulated, ground, and polished to 1 µm with diamond paste. Different degrees of etching were investigated to account for the specific microstructures of the SS and TS. The etching solutions included V2A-Beize, picric acid, and oxalic acid (electro etching; 20%, 2.7 V, 30 s, no current limit), using different exposure times (30–120 s).

The microstructure was evaluated on polished and etched cross-sections in both vertical and horizontal sections using a light optical microscope (LOM), namely the Nikon ECLIPSE L200 (Nikon, Tokyo, Japan), and a scanning electron microscope (SEM), namely a Tescan Vega and a Tescan Maia 3 (Tescan, Brno, Czech Republic), equipped with energy-dispersive X-ray spectroscopy (EDX) for elemental analysis. EDX analysis was performed on the polished cross-sections of selected specimens.

3.4. Local Micromechanical Tests (Nanoindentation)

To track local changes in the mechanical properties, nanoindentation experiments were conducted using an XP nanoindenter system (MTS, Oak Ridge, TN, USA). Grids of at least 4 × 4 indentations were created on selected specimens using a Berkovich-style tip calibrated on fused silica. Tests were performed under displacement control at penetration depths of h_{max} = 2000 nm. The local hardness and Young's modulus were calculated from the collected data using the model of Oliver and Pharr [53].

3.5. Macromechanical Hardness Tests (Rockwell)

Macroscopic Rockwell C tests were conducted in the cross-sections of functionally graded specimens to investigate the transitions in hardness. A Mitutoyo HR200 (Mitutoyo, Kanagawa, Japan) with a type C conical indenter was used for the tests. Profiles of indentations with a minimum of 3 tests per level were created across the cross-sections, with the minimum indent spacing of 2 mm and a dwell time of 5 seconds.

3.6. Sliding Contact Tests (Microscratch)

Microscratch tests were performed in a scratch tester unit (CSM-Instruments, now a part of Anton Paar, Needham Heights, MA, USA) with a 200-µm-radius spherical diamond indenter on the polished surfaces of selected specimens. The sliding tests were performed

under a linearly increasing load, from 0 to 120 N, at a loading rate of 4.2 mm/min and a scratch length of 5 mm.

4. Results and Discussion

4.1. Microstructural Analysis

The microstructural changes in the functionally graded specimens were evaluated in the selected specimens *cube* and *block* (see Figure 3). The transition in the microstructure across the cross-section of the specimen *cube* can be observed from the images in Figure 4. The micrographs correspond to an area near a lateral edge of the specimen. Due to the effects of etching, the different layers are visible in the low-magnification "stitched" image in Figure 4a. The gradual transition in the microstructure can be directly correlated with the brightening of the contrast in the material image (from right to left in Figure 4a) as the microstructure becomes gradually enriched in carbides towards the top TS-rich region (specifically, white contrasting Mo carbides). In the first few layers of the build, only SS and no carbide precipitation is observed (right-hand side of Figure 4a). As the build advances, the first carbide formations appear, and both Mo (white) and V (dark gray) carbides can be seen to precipitate along the columnar grain boundaries (higher-magnification image, Figure 4c). An increase in the carbide density is observed as new layers are added, until the top of the specimen is reached (left-hand side of Figure 4a), where the microstructure is composed of a complex network of eutectic-like Mo-rich carbides and isolated V-rich carbides dispersed in the matrix, as evident from Figure 4b. The high number of carbides in the TS-rich zone appears to break the elongated columnar grain growth formed in the initial SS-rich layers.

It is worth noting that the build strategy used yields a continuous material with no visible signs of cracks or significant porosity. The similarity in the process windows between the SS and TS, together with their compatibility in terms of the similar chemical composition (see Table 1) and thermal behavior (CTE_{SS}~16 μm $m^{-1}\,^{\circ}C^{-1}$ [54] and CTE_{TS}~11 μm $m^{-1}\,^{\circ}C^{-1}$, respectively, at 100 °C [55]), results in low residual stress concentration in the parts. The overall homogeneous nature of the microstructural transition indicates that a high degree of in situ alloying occurs in the specimen as it is manufactured. Focusing on each individual layer, it seems evident from Figure 4a that a higher concentration of carbides is aligned along the layer boundaries, probably due to remelting and melt pool fluid effects in combination with the specific heat distribution and solidification rate gradients.

Another interesting observation is that the microstructure in the vicinity of the edges resembles a composite-like situation (top of Figure 4a) where two phases coexist: round dark gray SS particles embedded within a white TS "matrix". The same microstructure was observed in a previous investigation when using PBF-EB to process 316L powders pre-blended with a highly alloyed Fe-based (Colferoloy) powder [16]. In the mentioned investigation, the outer surface areas (where the contour melting theme was used) resulted in a similar metal–metal composite material. Similar effects were observed in other systems, such as Cu-Fe [47], in which undercooling led to a metastable miscibility gap, resulting in liquid-phase separated materials. It can be speculated that the higher solidification rates in these specific areas, where the effect of remelting is less pronounced, together with lower local temperatures, result in insufficient thermal and physical conditions for in situ alloying. Isolated SS particles with a reduced diameter were also found in the bulk of the specimens, also aligned along the layer boundaries.

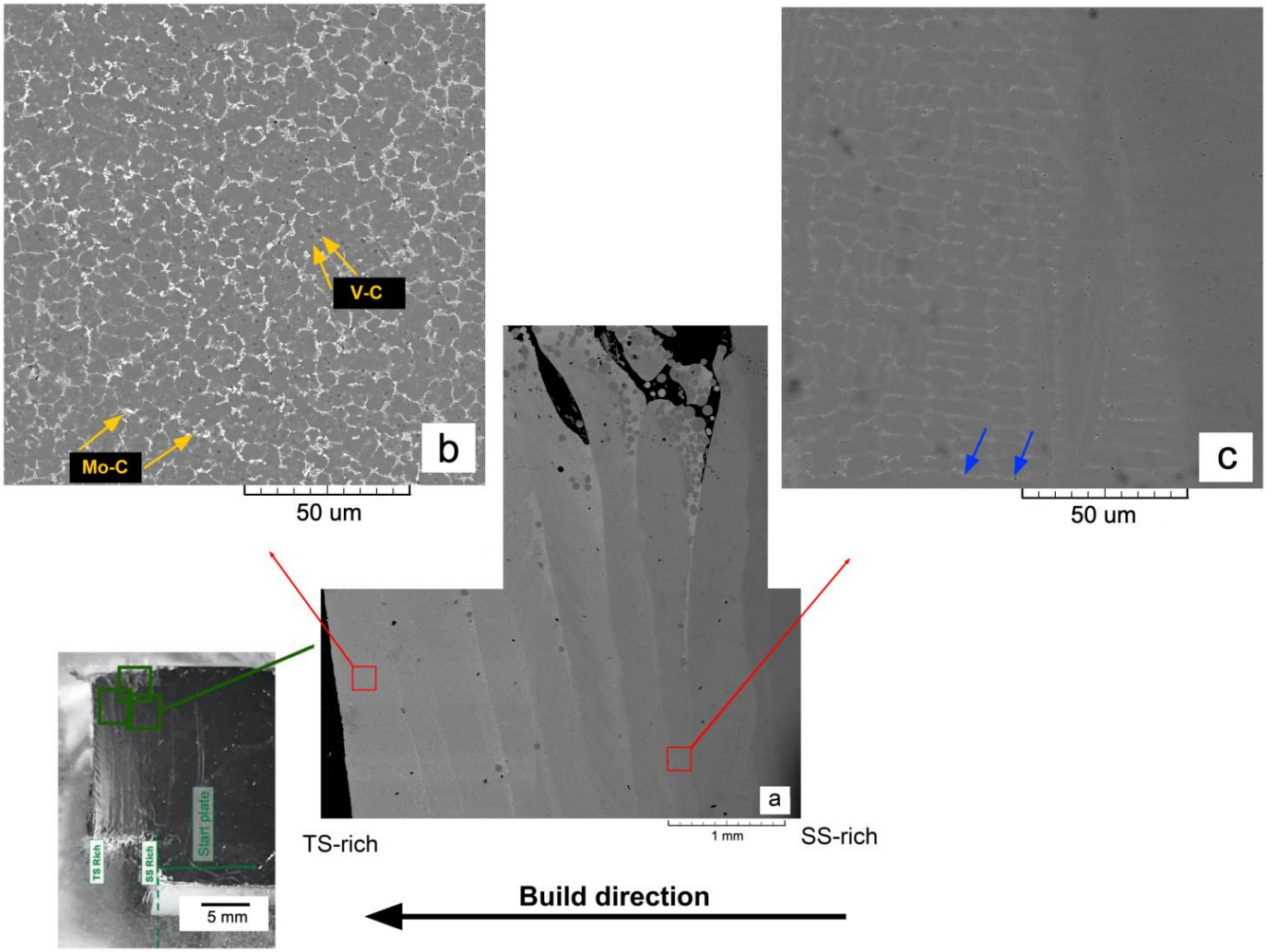

Figure 4. Changes in microstructure across the cross-section in the specimen *cube*—SS-rich zone to the right and TS-rich zone to the left of the images. The *cube* sample was built following *configuration I*. Montage of stitched low-magnification SEM images of different zones near one of the edges of the sample (**a**). Magnification of a zone near the bottom (**c**) and top (**b**) of the sample. Arrows in the micrographs (**b**,**c**) point to different carbide formations.

An image of the intensely etched cross-section of the sample "block", manufactured in the standard build setup following *configuration II*, is presented in Figure 5a. Clearly, the degree of etching with the same exposure time increases as the sample grows along the build direction, which is especially pronounced for the first 35 mm of the build (z = 0–35 mm). This is explained by the gradually decreasing SS content as it is slowly substituted by the less corrosion-resistant TS towards the top end of the sample. It can also be noticed that some variation in the etching degree happens from z~35 mm to the top of the specimen. Since the powder container used in the standard configuration is not symmetric, it is possible that "trapped" powder areas near the walls take longer periods of time to reach the deposited powder layer, causing some disturbance in powder disposal. In addition, the differences in the flowability and apparent density of the powders can play a role in the process of powder feeding during manufacturing.

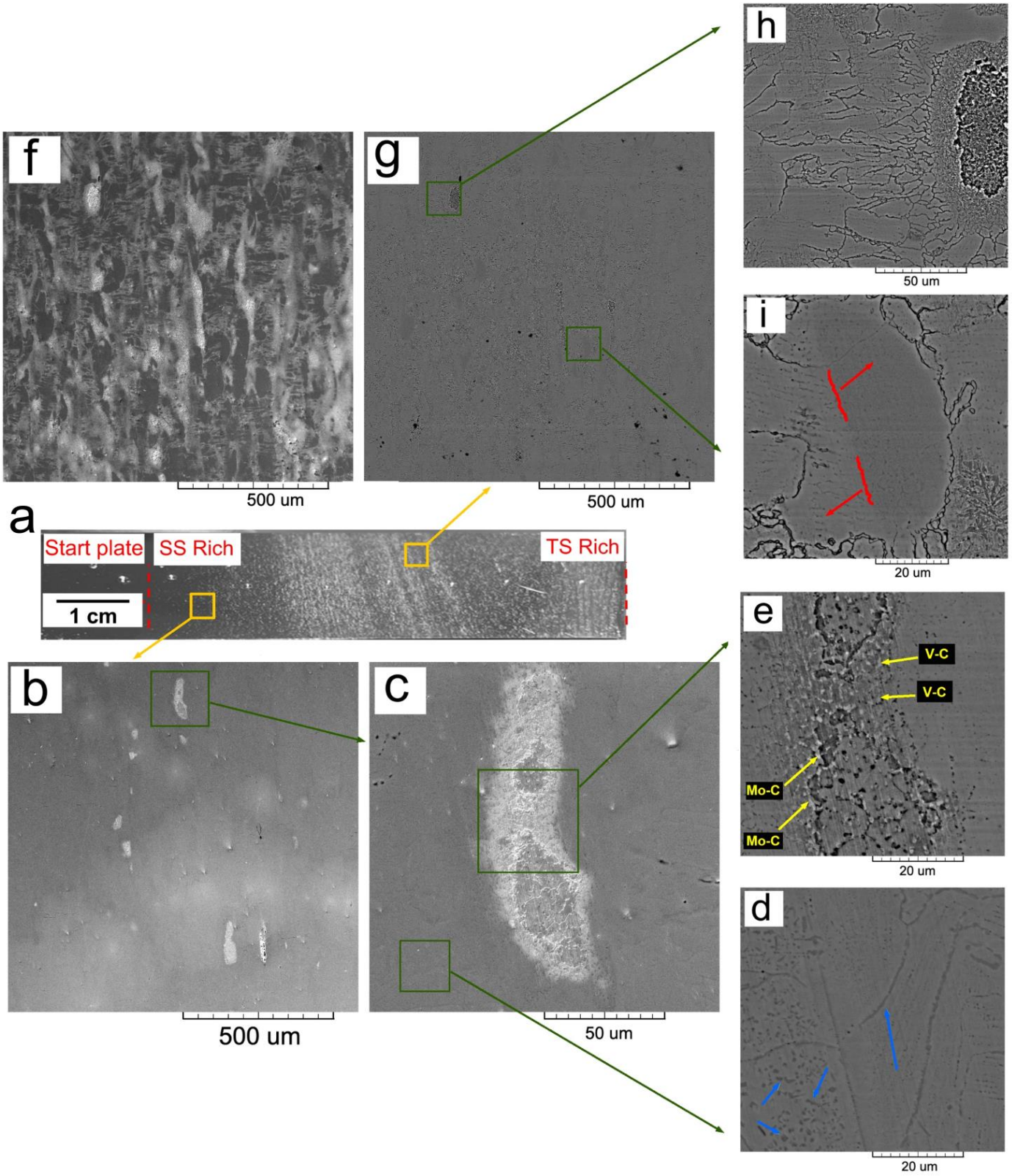

Figure 5. Changes in microstructure in an over-etched cross-section of the specimen *block*, as built following *configuration II*. General picture showing an overview of the cross-section (**a**). Higher-magnification SEM images taken from areas at z = 5 mm (**b**–**d**) and z = 30 mm (**f**–**i**). Arrows are added as insets and point to carbides in grain boundaries and inside grains (**d**) and clusters of Mo- and V-rich carbides in (**e**).

The low-magnification micrograph in Figure 5b outlines an area at 5 mm from the start plate (Z = 5 mm). It shows several isolated TS-rich islands (white contrasting areas) surrounded by a dark gray SS-rich matrix. Some of these islands with a reduced size appear in the SS matrix, forming a blurred "cloud" (light gray contrasted area), indicating some degree of in situ alloying. An area covering one of the islands is presented in the secondary electron (SE) contrast micrograph in Figure 5c. Higher-magnification micrographs using backscattered electron (BSE) contrast for SS-rich and TS-rich zones are shown in Figure 5d,e, respectively. The agglomeration of small Mo-rich (white) and V-rich (dark grey) carbides, clustered and forming TS-rich islands, is visible in the image in Figure 5e. A less etched SS-rich area with V-rich carbides decorating the grain boundaries is visible in Figure 5d. Another area of the cross-section in the TS-rich zone (at Z = 30 mm) is shown in the SE and BSE micrographs in Figure 5f,g, respectively. This zone is characterized by a higher density of white contrasting TS-rich islands in a less pronounced dark grey SS-rich matrix. It is clear that the microstructure is aligned in a columnar configuration along the build direction (z). The TS-rich islands showing a high degree of etching are again formed of small-sized carbide clusters, as shown in Figure 5h. The SS-rich zones are characterized by zones of variated grayscale contrast (because of due differential etching intensity), indicating a variating degree of in situ alloying, with carbides aligned along the grain boundaries. This is shown in the micrograph in Figure 5i.

Although gradual microstructural transitions were achieved for both specimens, a higher degree of in-situ alloying was observed for the sample *cube* (Figure 4) as compared with sample *block* (Figure 5). At this point, some factors deserve to be considered. Firstly, (i) in Figure 4a, it can be noticed that the energy is not sufficient close to the edges of the *cube* as the layers are not fully melted together. Here, it is also clear that, where the energy is insufficient, less alloying takes place (grains of TS are visible in SS matrix). (ii) Although the process temperature was approximately 850 °C for both build jobs, the heat retention is very different in the two samples. The *cube* has a small bulk volume and therefore is more sensitive to cooling by the slightly colder powder bed and when depositing new powder. Moreover, the small setup has less insulating powder around the start plate and a generally smaller thermal volume compared to a large build (both towards the chamber and each 50 µm powder layer). The *block*, on the other hand, has a relatively large bulk volume that can even out temperature fluctuations. This means that the *cube* needs a higher local temperature to sustain buildable conditions and thus both full-solution alloying and a composite material are visible in the sample. (iii) The transition from 100% SS to 100% TS occurs in a reduced volume of a few millimeters in the sample *cube* (z~5 mm) at a higher build temperature, whereas, for the sample *block*, the same transition occurs at z~40 mm. (iv) There is no intermediate blend of powders in between SS and TS for the sample *cube*, so the transition happens more drastically in a shorter time window.

4.2. Composition Analysis (EDX)

The variation in the elemental composition was studied using SEM-EDX along the cross-sections of the specimens *cube*, *block*, and *spring*. Since SS has significantly higher Cr content as compared to TS (see Table 1), and, conversely, since V is only present in TS, these two elements can be used as indicators of the compositional transients. It can be observed as a general trend among the measurements in all specimens (Figure 6a–c) that the Cr content decreases and the V content increases as the build progresses from the SS-rich initial layers near the start plate to the TS-rich ones at the samples' top surfaces. It should be noted that, because of the localized nature of the point EDX measurements and the heterogeneous nature of the microstructure in the specimens, these measurements are not absolute and must be interpreted as indications of trends. This is particularly true for

the sample *block*, shown in Figure 5 and discussed in Section 4.1, where a larger fluctuation in the V content is observed across the cross-section of the sample (see also Figure 5b).

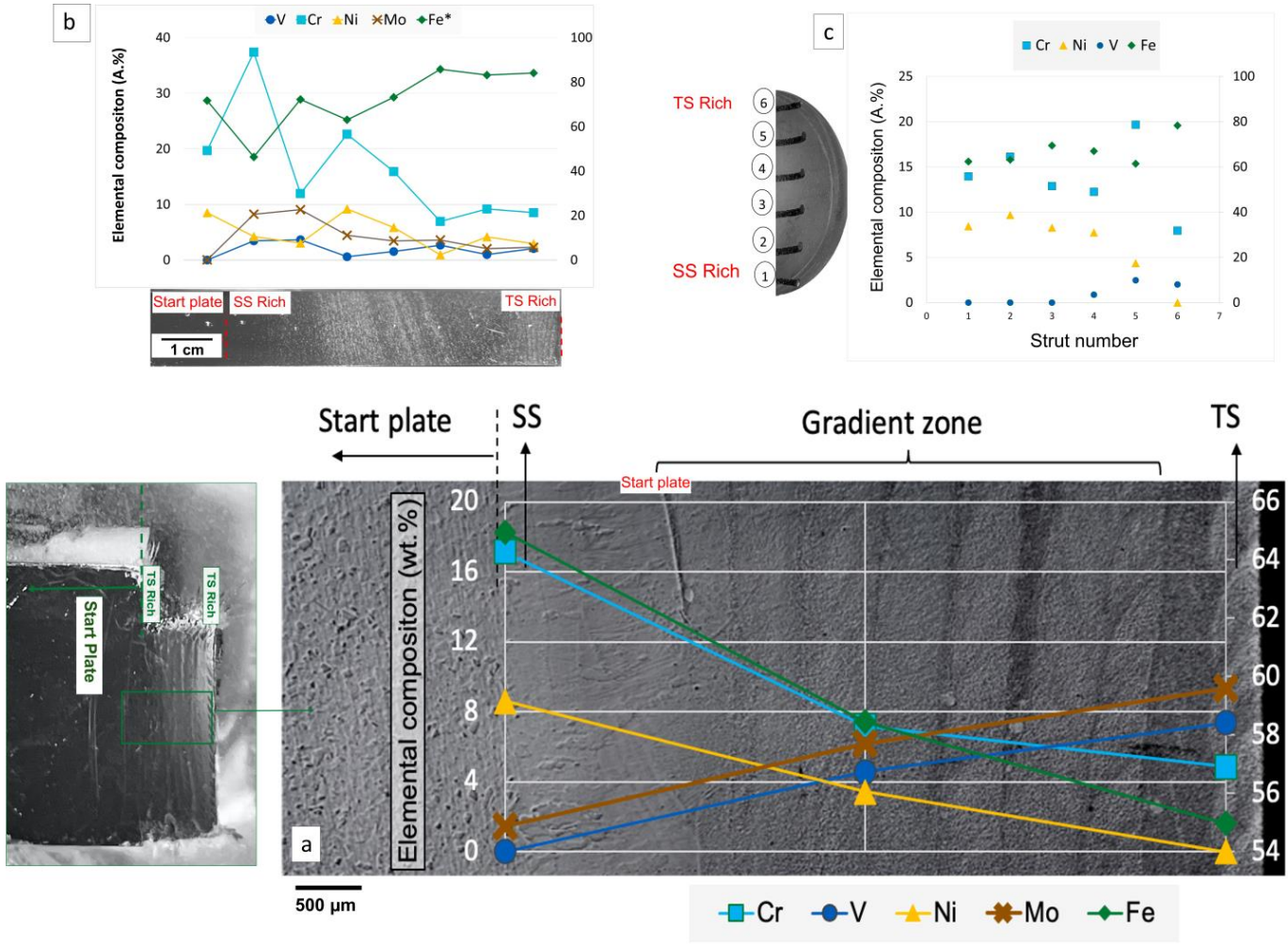

Figure 6. Compositional variations as measured using point measurements in SEM-EDX across the cross-sections of specimens *cube* (**a**), *block* (**b**), and *spring* (**c**). EDX point measurements are the average of at least 3 measurements acquired in regions corresponding to data points in (**a**–**c**). * Data for Fe in the plots refer to the secondary vertical axis.

The compositional results are, in general, in good agreement with the gradual transition in the microstructure for the materials built in *configuration I* and *configuration II*, i.e., vertical transitions from SS to TS along the build direction.

4.3. Local Mechanical Properties

4.3.1. Hardness

In order to investigate the local mechanical behavior of the functionally graded specimens, nanoindentation experiments were conducted both on the polished top and across cross-sections of the sample *cube*. In the SEM micrograph in Figure 7a, a grid of 4 × 4 nanoindentations created at the polished top surface of the sample *cube* is presented. The over-etching of the specimens was applied after the nanomechanical tests. A higher-magnification image of one of the indentation imprints is shown in Figure 7b. As the indentations were created on the top surface of the specimen, composed of TS-rich material, the underlying microstructure was composed of a eutectic-like network of Mo-rich carbides with isolated V-rich carbides, similar to the cross-sectional image in Figure 4b. The size

of the indentations followed the same length scale as the microstructure, so the effects of carbides were captured in the recorded response. The average hardness as a function of the penetration depth is plotted in the graph in Figure 7c. Stable hardness (H) values of around 10 GPa were found along the penetration regime.

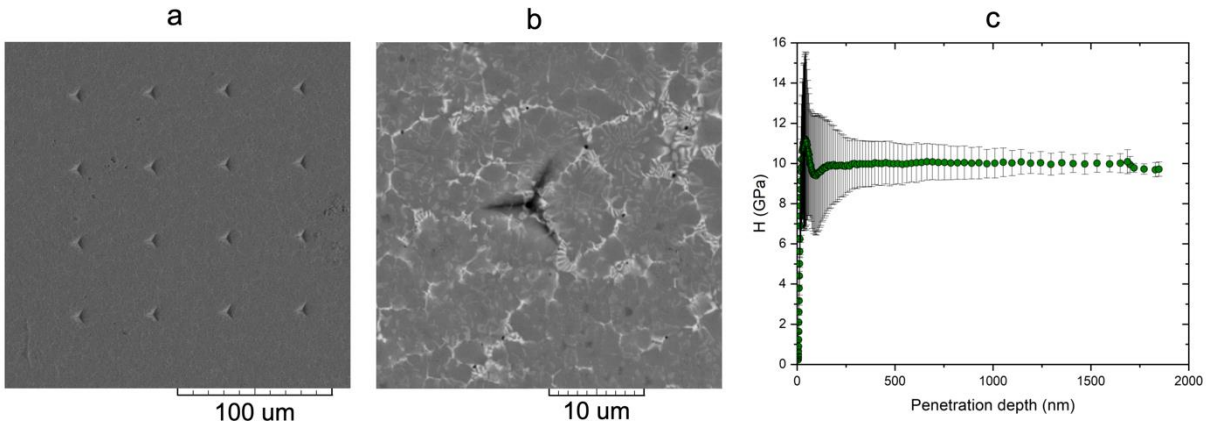

Figure 7. SEM micrographs of a 4 × 4 grid of nanoindentations created at the polished top surface of the sample *cube* (**a**). Higher-magnification image of one of the indentations (**b**). Average hardness (H) as a function of the penetration depth (**c**); standard deviation is included as error bars.

A profile with the nanoindentations forming a 4 × 33 grid was created on the cross-section of the *cube* specimen to track the local changes in the mechanical properties of the material. Figure 8a presents the changes in the nanohardness values across the functional gradient transition. Figure 8b presents an optical image of the nanoindentation grid. Figure 8c–e illustrate typical indentation imprints at different sample locations. Here, the bottom SS-rich areas of the specimen are located to the left in the image in Figure 8a (horizontal axis starting from 0), and TS-rich areas are located at the right side of the image (horizontal axis closer to 3.2 mm). A gradual increase in hardness can be observed in the graph (Figure 8a) as the material gradually changes from SS to TS. The hardness values evolve from H~4 GPa in the first few layers (bottom, SS) to H~10.5 GPa in the top layers (TS) (values comparable to the H values measured from the top surface; see Figure 7c). The hardness values recorded for the first SS-rich layers are similar to the values reported for the nanoindentation of 316L samples manufactured by PBF-EB [9,16]. The hardening of the material, as it is enriched in TS, can be explained by the combined action of three mechanisms directly related to the microstructure: the increase in the density of hard Mo-rich and V-rich carbides, the austenitic to martensitic transition in the parent matrix phase, and the effect of microstructure refinement due to the pinning of the columnar grain growth. The gradual increase in the density of carbides can be observed in the residual micrographs of selected nanoindentations in the SEM micrographs in Figure 8c–e.

4.3.2. Stiffness Measurements

The stiffness value, represented by an indentation elastic modulus (E), was also extracted from the nanoindentation experiments performed on the specimen *cube*. The average E value changes with the increasing indenter penetration depth, as measured on the polished TS-rich top surface of the specimens, are presented in Figure 9a. The results show stable E values of around 240 GPa. The evolution of E across the polished cross-section of the same specimen is presented in Figure 9b. As with the hardness values, gradual stiffening is observed as the material is enriched in TS. The stiffness values increase from E~180–200 GPa in the first SS-rich layers to E~230–250 GPa in the TS-rich zone near the top of the specimen (these values are in correspondence with the E values measured

in the experiments on the top surface). Again, the E values found here for the SS-rich materials in the first few layers are comparable to the previously reported ones for PBF-EB 316L samples [9,16].

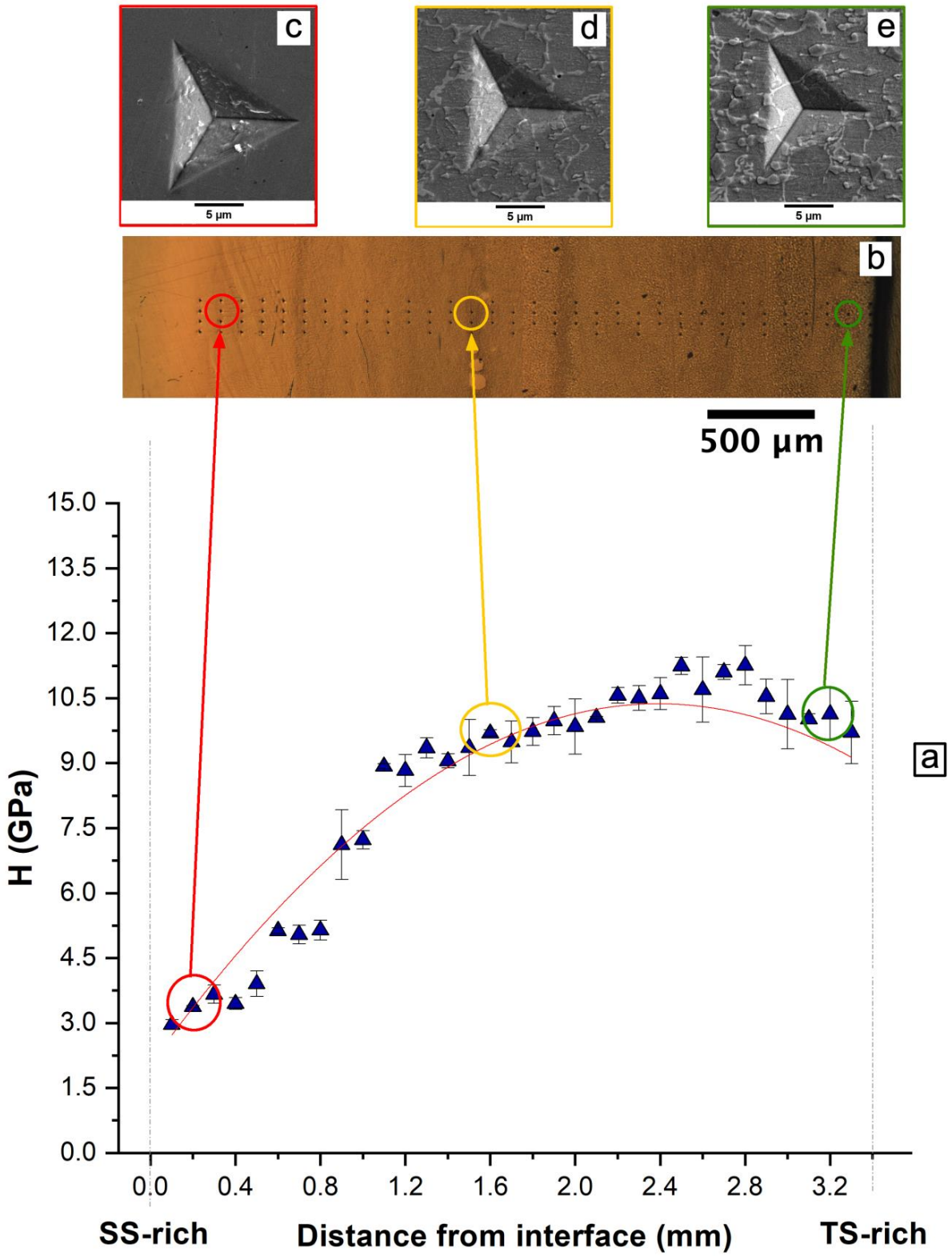

Figure 8. Average H profile of nanoindentations across the cross-section of the specimen *cube* (**a**); standard deviation from four measurements is included as error bars in each measurement. Optical micrograph showing an overview of the 4 × 33 grid of nanoindentations (**b**). Micrographs with residual imprints at selected locations across the profile (**c**–**e**).

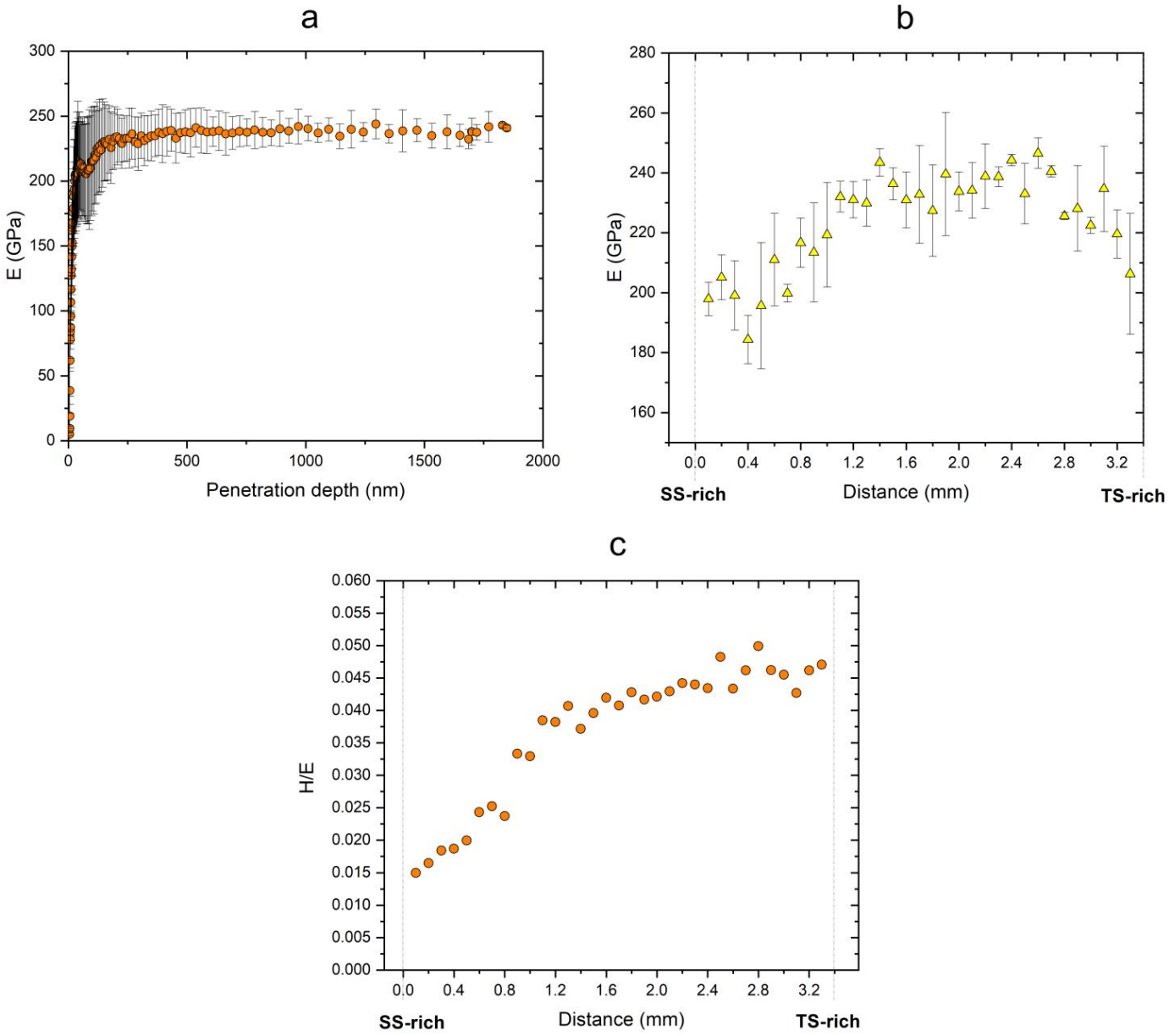

Figure 9. Average E as a function of the penetration depth from a 4 × 4 indentation grid at the top surface of the specimen *cube* (**a**); standard deviation is included as error bars. Average E profile of nanoindentations across the cross-section of the same specimen (**b**); standard deviation from 4 measurements is included as error bars in each measurement. (**b**) Plot H/E and comment on local wear ratio changes (**c**).

4.3.3. Wear Ratio (H/E)

An indirect measure of the wear behavior can be extracted from the H/E ratio (also called the wear ratio). The average H/E values extracted based on the measurements in the cross-section of the sample *cube* are presented in Figure 9c. The average wear ratio also increases gradually from H/E 0.015 to 0.045 as the material becomes richer in TS.

4.4. Macromechanical Properties

4.4.1. Rockwell Hardness

Macroscopic Rockwell experiments were also performed to track changes in the macro-hardness of the specimens, as well as to investigate the material deformation mechanisms under contact loading. Although the Rockwell C scale (HRC) is not the best-suited one for

SS, it was used for the comparison to account for the values expected for TS. A profile of the HRC measurements across the section of the sample *block* is plotted as a function of the distance from the start plate in Figure 10a, together with characteristic indentation imprints at different locations (Figure 10b–e). Here, the first layers of the SS-rich zone are located to the left (z close to 0) and the TS-rich top zone of the specimen (z nearing 35 mm) to the right. Again, the gradual hardening of the specimen is observed along the build direction as the TS content increases. From the SEM micrographs in Figure 10b–e, it can be readily observed how the diameter of the residual imprints decreases with the distance from the start plate. From the same images, the progression of the microstructure can be discerned in the background of the residual imprints. The density of TS-rich islands (also rich in Mo- and V-carbides) increases towards the top surface.

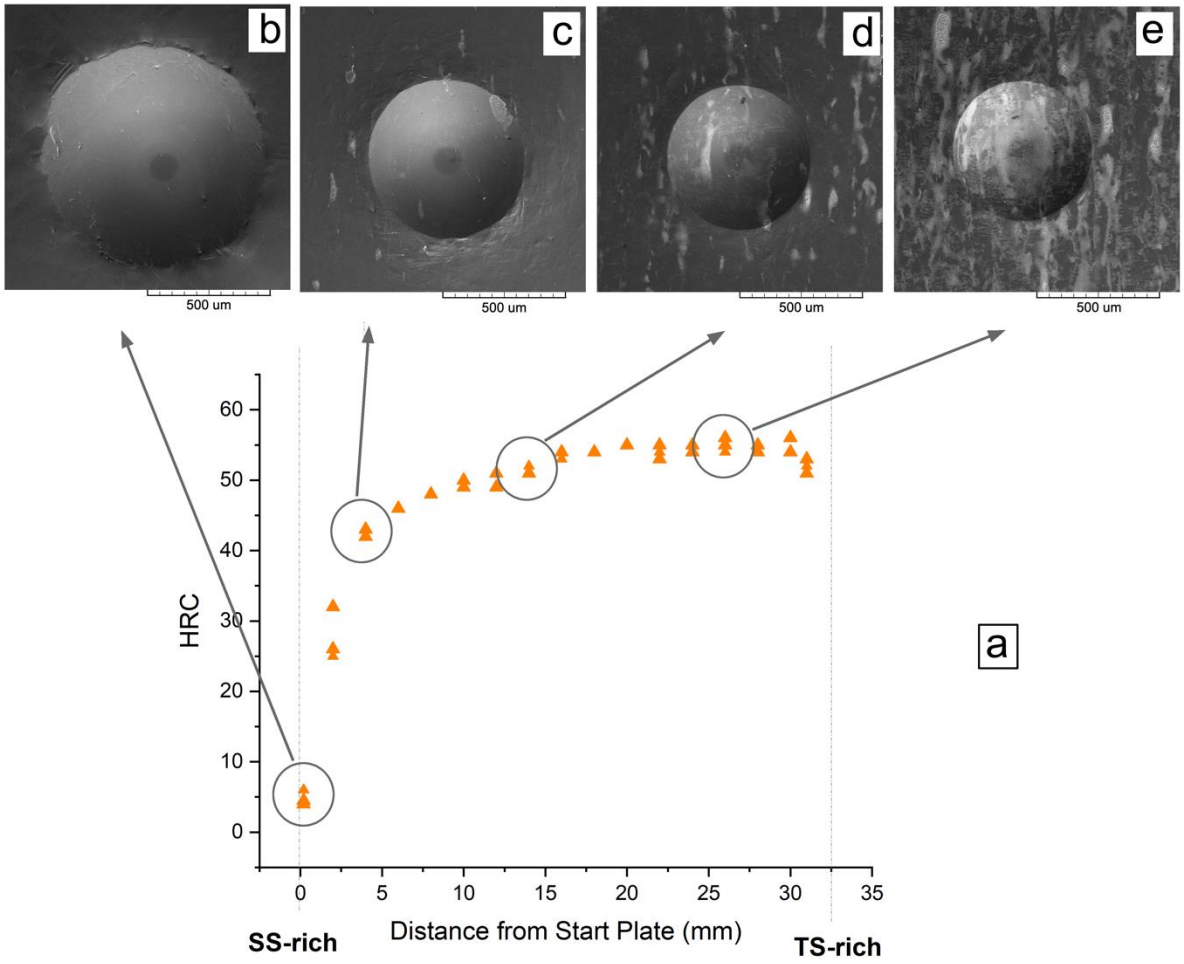

Figure 10. HRC profile across the cross-section of the specimen *block* as a function of the distance from the start plate (**a**). Micrographs showing the evolution in the residual imprints across the profile for selected experiments (**b**–**e**).

Furthermore, it is worth noticing the evolution in the deformation mechanisms under the static contact loading conditions applied in the Rockwell experiments. In the tests carried out at the interphase with the start plate (Figure 10b), and in the SS-rich zone (Figure 10c), a highly plastically deformed area can be observed around the contours of the residual imprints, where the material is subjected to both axial and compressive stresses. The optical micrograph in Figure 11a, also taken from an indentation imprint test on the SS-rich zone, allows us to identify more clearly the damage at the peripheries of the imprints. In these areas, slip deformation is present, forming slip bands in grains near the indentation

edge (indicated by arrows in Figure 11a). Comparable slip deformation mechanisms have been reported for additively manufactured 316L samples under monotonic loading conditions after a tensile test [56]. As the carbide density increases towards the top TS-rich surface, the hardening mechanisms previously discussed are activated, and the slip deformation is significantly reduced as the movement of the matrix is increasingly restricted by the presence of carbides (Figure 10c), until it virtually disappears in the SEM micrographs (see Figure 10d). The optical micrograph in Figure 11b of the nanoindentation imprint in the TS-rich zone allows the identification of minor signs of residual plastic mechanisms of deformation confined to areas near the edges of the imprints, as indicated by the arrows.

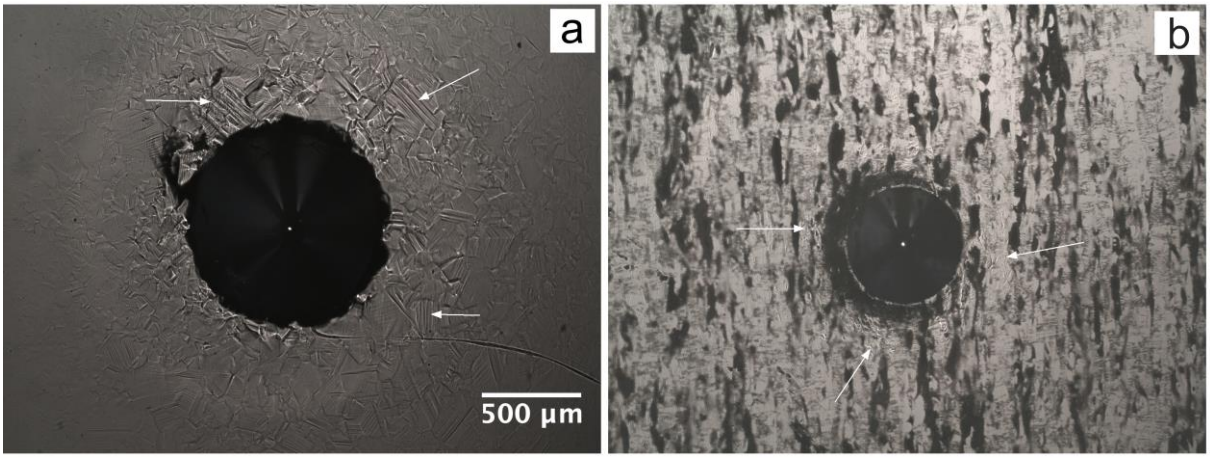

Figure 11. Residual tracks of Rockwell experiments in the SS-rich (**a**) and TS-rich (**b**) areas on the polished cross-sections of the *block* specimen. Both micrographs have the same scale. The arrows point to deformation behavior (slip planes in (**a**) and residual plastic mechanisms of deformation in (**b**)).

4.4.2. Sliding Contact Resistance

The resistance of the FGM to sliding contact was also investigated using scratch tests. The plots in Figure 12a represent the penetration profiles acquired during the scratches performed at different zones in the cross-section of the specimen *block* from the start plate to the top TS-rich zone. For a given scratch length, the penetration depth decreases as the material is gradually enriched in TS, as would be expected due to the consequent and progressive hardening. The sequence of micrographs of Figure 12b–e, focused on the top end of the residual tracks (maximum load), shows the evolution of the surface damage along the sample cross-section. Due to the increase in hardness, the width of the tracks decreases towards the TS-rich top surface. It is interesting that slip deformation zones, similar to those found around the Rockwell residual imprints, are also evidenced at the peripheries of the scratch tracks. These areas are especially marked around the top end of the tracks, where the maximum load is applied, and they significantly decrease in size from the scratch at the start plate (Figure 12b) to the one at the SS-rich zone (see Figure 12c), until they virtually disappear in the transition and TS-rich zones (Figure 12d,e, respectively). Another interesting observation is that small cracks appear in the internal cavity of the residual track of the scratch created in the SS-rich zone. The size and density of these cracks increase in the scratches created at the transition and TS-rich zones. Gradual evolution in the damage caused because of the sliding contact tests is observed—from ductile behavior, where mostly plastic deformation occurs in the residual tracks in the SS-rich bottom zone, to brittle behavior, where increasing cracking appears inside the tracks towards the TS-rich top zone. Such behavior is in agreement with the indications provided by the differences in the H/E ratio.

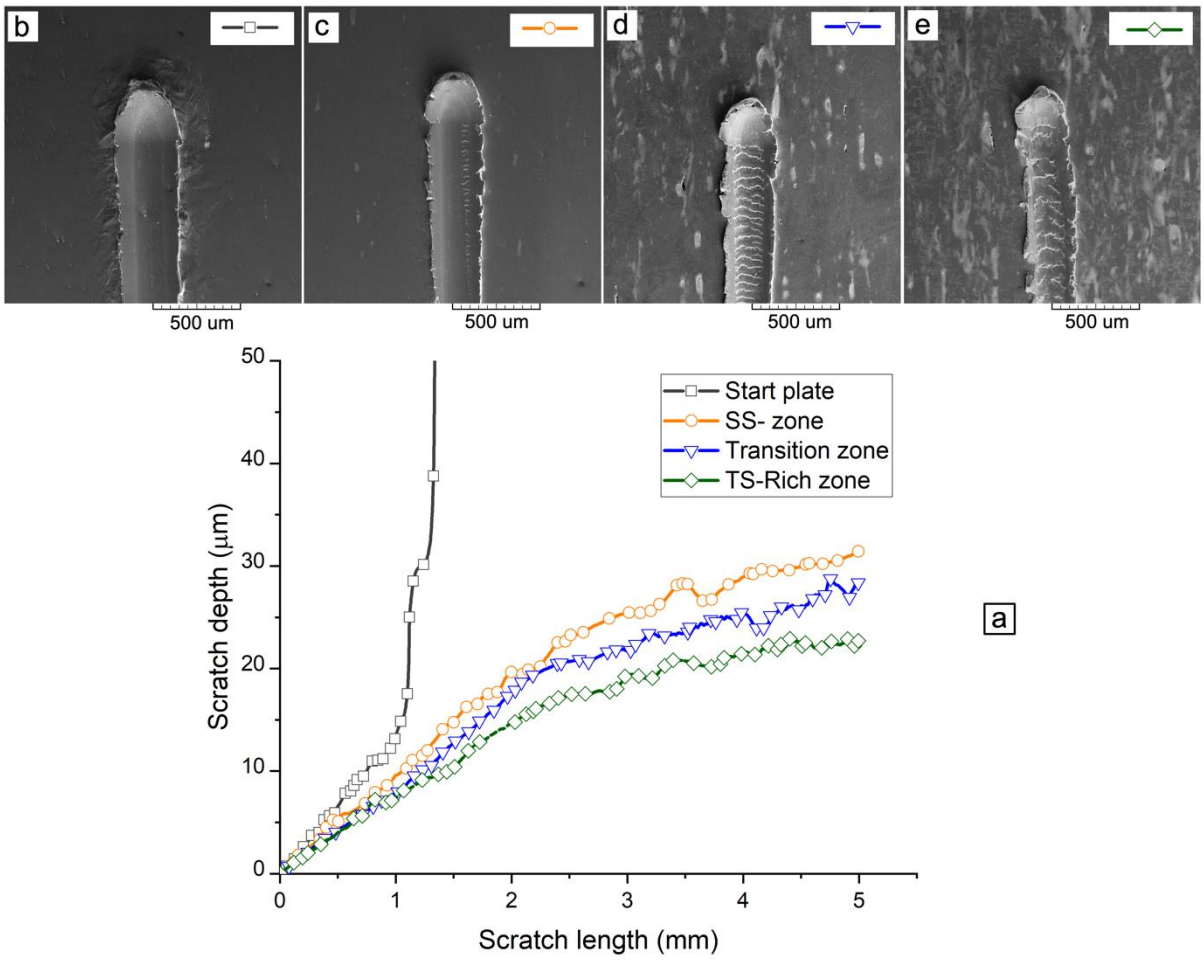

Figure 12. Plots of scratch depth vs. scratch length for different experiments carried out along the cross-section of the specimen *block* (**a**). SEM micrographs of the residual tracks focused at the top end of selected scratches: at the start plate (**b**), in an SS-rich zone (**c**), in the transition zone (**d**), and in a TS-rich zone (**e**).

4.5. Demonstrators

The approach proposed in this investigation allows us to gradually combine the intrinsic properties of two different materials within the same component. Furthermore, this is achieved in a single process using PBF-EB, a metal AM technology that allows for the manufacturing of complex parts with intricate geometries and the tailoring of the manufacturing process parameters. Within this context, two demonstrators were manufactured in which the functionality was tailored by a combination of the gradual changes in the materials and the geometry of the components: a progressive stiffness spring and a hardness-tailored punch.

4.5.1. Progressive Stiffness Spring

To evaluate the local changes in the intrinsic stiffness with the compositional gradient, nanoindentation experiments were conducted on the polished cross-sections of individual turns of the sample *spring* (built following *configuration II*; see Figure 3b). The residual imprints after the tests on turn 1 (SS-rich zone) are shown in the SEM micrograph in Figure 13a; for turn 3 (transition zone) in Figure 13b; and for turn 6 (TS-rich zone) in Figure 13c. The gradual transition in the microstructure from the SS-rich material with no carbides (Figure 13a) to the TS-rich material with both Mo and V carbides (Figure 13c) is evident.

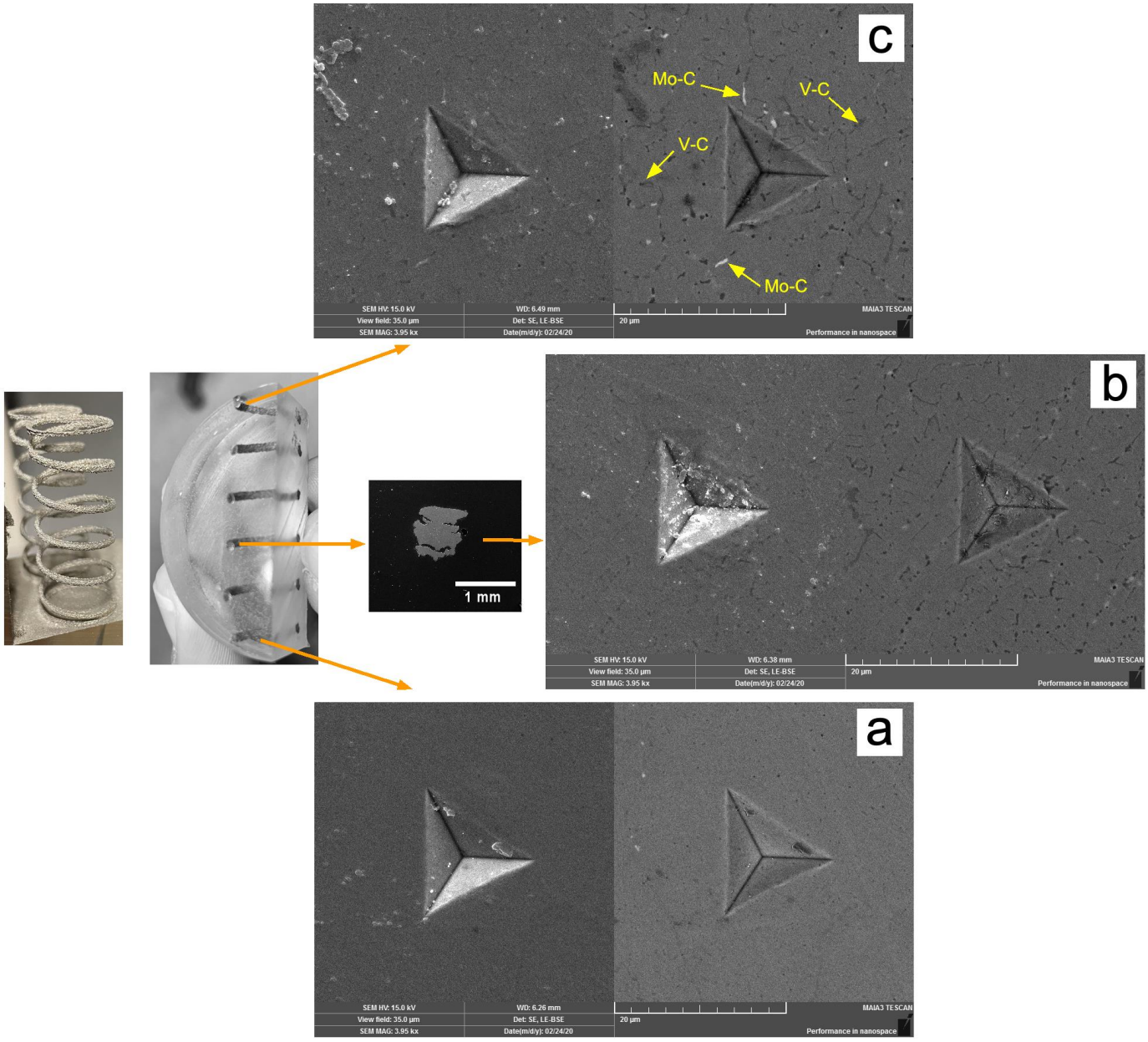

Figure 13. Montage with SE and BSE micrographs of residual nanoindentation imprints in different struts along the build direction for the specimen *spring*, from strut 1 in the SS-rich zone (**a**), to strut 3 in the transition zone (**b**), to strut 6 in the TS-rich zone (**c**).

The variation in stiffness, expressed in terms of E, is presented in Figure 14 as a function of the turn number, which increases as the specimen is built from SS-rich to TS-rich material. Despite the high values observed in strut 3, probably due to the localization of the indents in a TS concentration zone due to the heterogeneous nature of the microstructure, the gradual progression of the stiffness is recorded, ranging from E values comparable to those of the SS (average E~195 GPa) to E values attributable to TS (average E~245 GPa). As the macroscopic elastic response of the spring is a combination of the intrinsic material properties and the geometry, the approach proposed here permits us to functionalize the response of the spring by both tailoring the intrinsic elastic response, as E is progressively tailored from a more compliant material at one end to a stiffer one at the other, and the specific geometric design.

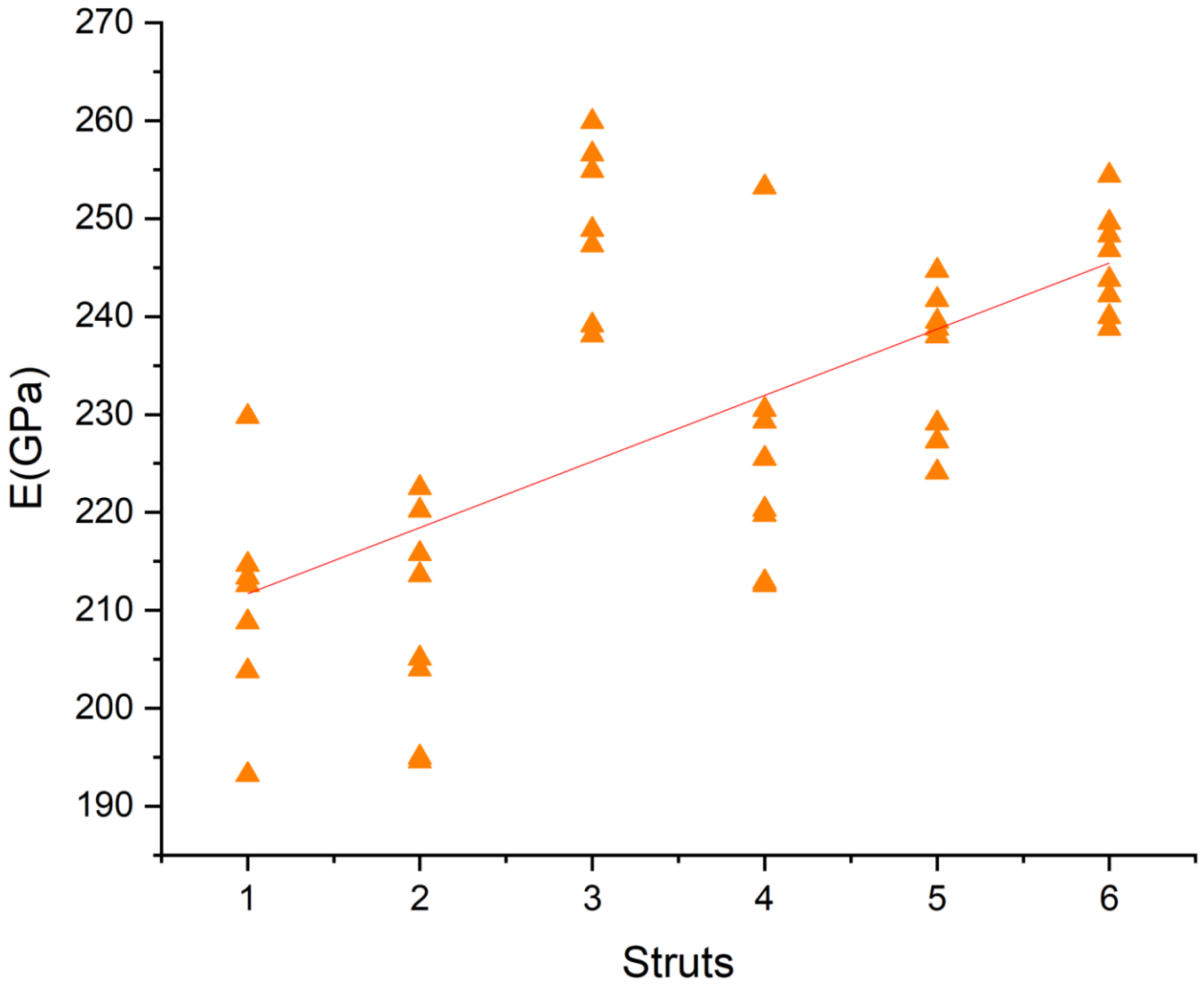

Figure 14. Stiffness (E) variation with the gradual material transition across struts 1–6 (d); see Figure 13.

4.5.2. Hardness-Tailored Punching Tool

A punching tool was manufactured using *configuration III* (TS/TS + SS/SS; see Figure 3c). The cross-section of the punch (see details in Figure 15a) was prepared for microstructure and hardness analysis, as depicted in the optical and SEM micrographs in Figure 15b–h. The sequence of stitched images in Figure 15b–f shows higher-magnification areas of the top or "head" of the punch. The transition in the microstructure from the start plate (left-hand side in Figure 15b) to the SS-rich zone (right-hand side in Figure 15f) is distinguishable from the images. After the intense etching of the sample, a dark-contrasted TS-rich material can be observed, as in Figure 15a, in the first layers of the punch, as the build layers progress from the start plate. The gradual brightening in Figure 15c indicates some degree of in situ alloying as the powder supplied to consecutive layers gradually changes from only TS to the TS + SS blend. As observed from Figure 6, and discussed earlier in Section 4.1 for the sample *block*, isolated TS-rich islands (dark) embedded in an SS-rich matrix (bright) start to appear in the middle of the transition zone (Figure 15d). This area is also presented in the SEM micrographs in Figure 15g–h, where the TS-rich islands are bright-contrasted. As the powder being fed to the table switches from TS + SS to SS, the

density of the TS-rich islands gradually declines until they disappear (Figure 14e,f), and the core or "bulk" of the punch is built of only SS.

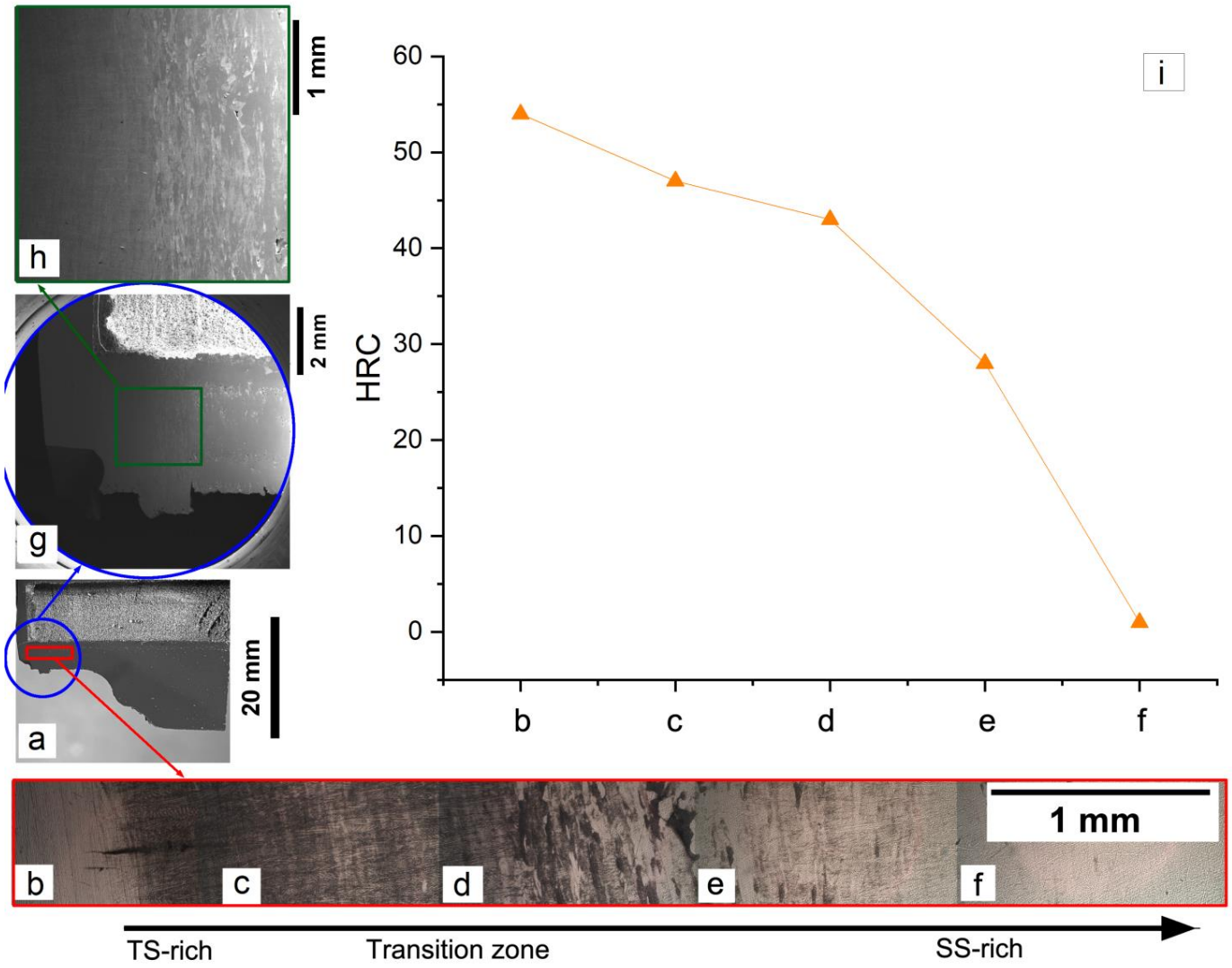

Figure 15. Cross-section of the specimen "punch" (**a**). Optical (**b**–**f**) and SEM micrographs (**g**,**h**), in over-etched sample condition, showing the gradual microstructural transitions. Graph (**i**) showing the variation in Rockwell hardness with the distance from the start plate, as measured in areas corresponding to the optical images (**b**–**f**).

Figure 15i presents the profile of the Rockwell hardness measured along the cross-section of the punch. A gradual transition in hardness is recorded from the hard punch head, with hardness values characteristic of TS (H~54 HRC, similar to the specimen *block* and references [13,14]), to a soft punch core, with hardness values comparable to the ones measured for SS.

In metal-forming processes, it is often desirable to use a hard material at the forming edge of the tools and a more ductile material in the core. This is usually achieved by combining different materials, which, as mentioned before, might be problematic from a process and materials perspective. In this example, it is demonstrated how the combination of materials (SS and TS), together with the successive powder feeding and design freedom of AM (PBF-EB), may be used to achieve functionalized components (punching tool), where the properties (hardness) are gradually tailored for increased performance.

5. Conclusions

This study presents an innovative approach consisting of successive powder feeding in powder bed additive manufacturing (PBF-EB) to achieve FGMs by combining two different steel powders, with marked differences in their mechanical properties. Extensive chemical, microstructural, and macro- and nano-mechanical analyses reveal a gradual transition within the materials, from the soft and ductile stainless steel to the hard, stiff, and wear-resistant tool steel. This transition occurs in a continuous manner, with no evidence of structural failure, cracking, or induced porosity. The results of this research demonstrate how the combination of materials, and the design freedom offered by additive manufacturing, can be utilized to create functionalized components, such as a punching tool or a progressive spring, where properties like the hardness and stiffness can be gradually engineered to enhance their performance.

Author Contributions: Conceptualization and methodology, C.B., W.S. and A.K.; validation, C.B.; formal analysis, W.S. and C.B.; investigation, C.B. and E.J.-P.; resources, L.-E.R.; writing—original draft preparation, C.B.; writing—review and editing, W.S.; visualization, C.B.; supervision, L.-E.R.; project administration, L.-E.R. All authors have read and agreed to the published version of the manuscript.

Funding: This research received no external funding.

Data Availability Statement: The authors confirm that the data supporting the findings of this study are available within the article. Additional data, build logs, etc., may be shared upon request to the authors.

Conflicts of Interest: The authors declare no conflicts of interest.

References

1. Tamayo, J.A.; Riascos, M.; Vargas, C.A.; Baena, L.M. Additive manufacturing of Ti6Al4V alloy via electron beam melting for the development of implants for the biomedical industry. *Heliyon* **2021**, *7*, e06892. [CrossRef] [PubMed]
2. Knörlein, J.; Franke, M.M.; Schloffer, M.; Körner, C. In-situ aluminum control for titanium aluminide via electron beam powder bed fusion to realize a dual microstructure. *Addit. Manuf.* **2022**, *59*, 103132. [CrossRef]
3. Murr, L.E.; Martinez, E.; Gaytan, S.M.; Ramirez, D.A.; Machado, B.I.; Shindo, P.W.; Martinez, J.L.; Medina, F.; Wooten, J.; Ciscel, D.; et al. Microstructural architecture, microstructures, and mechanical properties for a nickel-base superalloy fabricated by electron beam melting. *Metall. Mater. Trans. A Phys. Metall. Mater. Sci.* **2011**, *42*, 3491–3508. [CrossRef]
4. Helmer, H.E.; Körner, C.; Singer, R.F. Additive manufacturing of nickel-based superalloy Inconel 718 by selective electron beam melting: Processing window and microstructure. *J. Mater. Res.* **2014**, *29*, 1987–1996. [CrossRef]
5. Kirka, M.M.; Medina, F.; Dehoff, R.; Okello, A. Mechanical behavior of post-processed Inconel 718 manufactured through the electron beam melting process. *Mater. Sci. Eng. A* **2017**, *680*, 338–346. [CrossRef]
6. Ramsperger, M.; Eichler, S. Electron Beam Based Additive Manufacturing of Alloy 247 for Turbine Engine Application: From Research towards Industrialization. *Metall. Mater. Trans. A Phys. Metall. Mater. Sci.* **2023**, *54*, 1730–1743. [CrossRef]
7. Hong, J.H.; Yeoh, F.Y. Mechanical properties and corrosion resistance of cobalt-chrome alloy fabricated using additive manufacturing. *Mater. Today Proc.* **2020**, *29*, 196–201. [CrossRef]
8. Roos, S.; Rännar, L.E. Process window for electron beam melting of 316ln stainless steel. *Metals* **2021**, *11*, 137. [CrossRef]
9. Roos, S.; Botero, C.; Danvind, J.; Koptioug, A.; Rännar, L.E. Macro- and Micromechanical Behavior of 316LN Lattice Structures Manufactured by Electron Beam Melting. *J. Mater. Eng. Perform.* **2019**, *28*, 7290–7301. [CrossRef]
10. Zhong, Y.; Rännar, L.-E.; Liu, L.; Koptyug, A.; Wikman, S.; Olsen, J.; Cui, D.; Shen, Z. Additive manufacturing of 316L stainless steel by electron beam melting for nuclear fusion applications. *J. Nucl. Mater.* **2017**, *486*, 234–245. [CrossRef]
11. Rännar, L.E.; Koptyug, A.; Olsén, J.; Saeidi, K.; Shen, Z. Hierarchical structures of stainless steel 316L manufactured by Electron Beam Melting. *Addit. Manuf.* **2017**, *17*, 106–112. [CrossRef]
12. Roos, S.; Botero, C.; Rännar, L.E. Electron beam powder bed fusion processing of 2507 super duplex stainless steel. as-built phase composition and microstructural properties. *J. Mater. Res. Technol.* **2023**, *24*, 6473–6483. [CrossRef]
13. Botero, C.; Ramsperger, M.; Selte, A.; Åsvik, K.; Koptyug, A.; Skoglund, P.; Roos, S.; Rännar, L.-E.; Bäckström, M. Additive Manufacturing of a Cold-Work Tool Steel using Electron Beam Melting. *Steel Res. Int.* **2019**, *91*, 1900448. [CrossRef]

14. Botero, C.A.; Şelte, A.; Ramsperger, M.; Maistro, G.; Koptyug, A.; Bäckström, M.; Sjöström, W.; Rännar, L.-E. Microstructural and mechanical evaluation of a cr-mo-v cold-work tool steel produced via electron beam melting (Ebm). *Materials* **2021**, *14*, 2963. [CrossRef]
15. Koptyug, A.; Bäckström, M.; Vega, C.A.B.; Popov, V.; Chudinova, E. Developing new materials for electron beam melting: Experiences and challenges. *Mater. Sci. Forum* **2018**, *941*, 2190–2195. [CrossRef]
16. Koptyug, A.; Popov, V.V.; Vega, C.A.B.; Jiménez-Piqué, E.; Katz-Demyanetz, A.; Rännar, L.-E.; Bäckström, M. Compositionally-tailored steel-based materials manufactured by electron beam melting using blended pre-alloyed powders. *Mater. Sci. Eng. A* **2020**, *771*, 138587. [CrossRef]
17. Singh, D.D.; Arjula, S.; Reddy, A.R. Functionally Graded Materials Manufactured by Direct Energy Deposition: A review. *Mater. Today Proc.* **2021**, *47*, 2450–2456. [CrossRef]
18. Loh, G.H.; Pei, E.; Harrison, D.; Monzón, M.D. An overview of functionally graded additive manufacturing. *Addit. Manuf.* **2018**, *23*, 34–44. [CrossRef]
19. Ghanavati, R.; Naffakh-Moosavy, H. Additive manufacturing of functionally graded metallic materials: A review of experimental and numerical studies. *J. Mater. Res. Technol.* **2021**, *13*, 1628–1664. [CrossRef]
20. Hu, Z.; Ma, Z.; Yu, L.; Liu, Y. Functionally graded materials with grain-size gradients and heterogeneous microstructures achieved by additive manufacturing. *Scr. Mater.* **2022**, *226*, 115197. [CrossRef]
21. Knieps, M.S.; Reynolds, W.J.; Dejaune, J.; Clare, A.T.; Evirgen, A. In-situ alloying in powder bed fusion: The role of powder morphology. *Mater. Sci. Eng. A* **2021**, *807*, 140849. [CrossRef]
22. Katz-Demyanetz, A.; Popov, V.V.; Kovalevsky, A.; Safranchik, D.; Koptyug, A. Powder-bed additive manufacturing for aerospace application: Techniques, metallic and metal/ceramic composite materials and trends. *Manuf. Rev.* **2019**, *6*, 5. [CrossRef]
23. Svetlizky, D.; Zheng, B.; Vyatskikh, A.; Das, M.; Bose, S.; Bandyopadhyay, A.; Schoenung, J.M.; Lavernia, E.J.; Eliaz, N. Laser-based directed energy deposition (DED-LB) of advanced materials. *Mater. Sci. Eng. A* **2022**, *840*, 142967. [CrossRef]
24. Mosallanejad, M.H.; Niroumand, B.; Aversa, A.; Saboori, A. In-situ alloying in laser-based additive manufacturing processes: A critical review. *J. Alloy. Compd.* **2021**, *872*, 159567. [CrossRef]
25. Li, W.; Chen, X.; Yan, L.; Zhang, J.; Zhang, X.; Liou, F. Additive manufacturing of a new Fe-Cr-Ni alloy with gradually changing compositions with elemental powder mixes and thermodynamic calculation. *Int. J. Adv. Manuf. Technol.* **2017**, *95*, 1013–1023. [CrossRef]
26. Wang, C.; Tan, X.; Du, Z.; Chandra, S.; Sun, Z.; Lim, C.; Tor, S.; Lim, C.; Wong, C. Additive manufacturing of NiTi shape memory alloys using pre-mixed powders. *J. Mater. Process Technol.* **2019**, *271*, 152–161. [CrossRef]
27. Kim, D.K.; Woo, W.; Kim, E.Y.; Choi, S.H. Microstructure and mechanical characteristics of multi-layered materials composed of 316L stainless steel and ferritic steel produced by direct energy deposition. *J. Alloy. Compd.* **2018**, *774*, 896–907. [CrossRef]
28. Zhang, C.H.; Zhang, H.; Wu, C.L.; Zhang, S.; Sun, Z.L.; Dong, S.Y. Multi-layer functional graded stainless steel fabricated by laser melting deposition. *Vacuum* **2017**, *141*, 181–187. [CrossRef]
29. Charan, M.S.; Naik, A.K.; Kota, N.; Laha, T.; Roy, S. Review on developments of bulk functionally graded composite materials. *Int. Mater. Rev.* **2022**, *67*, 797–863. [CrossRef]
30. Carroll, B.E.; Otis, R.A.; Borgonia, J.P.; Suh, J.-O.; Dillon, R.P.; Shapiro, A.A.; Hofmann, D.C.; Liu, Z.-K.; Beese, A.M. Functionally graded material of 304L stainless steel and inconel 625 fabricated by directed energy deposition: Characterization and thermodynamic modeling. *Acta Mater.* **2016**, *108*, 46–54. [CrossRef]
31. Li, W.; Karnati, S.; Kriewall, C.; Liou, F.; Newkirk, J.; Taminger, K.M.B.; Seufzer, W.J. Fabrication and characterization of a functionally graded material from Ti-6Al-4V to SS316 by laser metal deposition. *Addit. Manuf.* **2017**, *14*, 95–104. [CrossRef]
32. Wits, W.W.; Amsterdam, E. Graded structures by multi-material mixing in laser powder bed fusion. *CIRP Ann.* **2021**, *70*, 159–162. [CrossRef]
33. Vora, P.; Mumtaz, K.; Todd, I.; Hopkinson, N. AlSi12 in-situ alloy formation and residual stress reduction using anchorless selective laser melting. *Addit. Manuf.* **2015**, *7*, 12–19. [CrossRef]
34. Uhlmann, E.; Bergmann, A.; Gridin, W. Investigation on Additive Manufacturing of Tungsten Carbide-cobalt by Selective Laser Melting. *Procedia CIRP* **2015**, *35*, 8–15. [CrossRef]
35. Radulov, I.; Popov, V.; Koptyug, A.; Maccari, F.; Kovalevsky, A.; Essel, S.; Gassmann, J.; Skokov, K.; Bamberger, M. Production of net-shape Mn-Al permanent magnets by electron beam melting. *Addit. Manuf.* **2019**, *30*, 100787. [CrossRef]
36. Popov, V.V.; Katz-Demyanetz, A.; Koptyug, A.; Bamberger, M. Selective electron beam melting of Al0.5CrMoNbTa0.5 high entropy alloys using elemental powder blend. *Heliyon* **2019**, *5*, e01188. [CrossRef] [PubMed]
37. Feng, L.; Wenjun, G.; Chao, G. Microstructures of Components Synthesized via Electron Beam Selective Melting Using Blended Pre-Alloyed Powders of Ti6Al4V and Ti45Al7Nb. *Rare Met. Mater. Eng.* **2015**, *44*, 2623–2627.
38. Surmeneva, M.A.; Koptyug, A.; Khrapov, D.; Ivanov, Y.F.; Mishurova, T.; Evsevleev, S.; Prymak, O.; Loza, K.; Epple, M.; Bruno, G.; et al. In situ synthesis of a binary Ti–10at% Nb alloy by electron beam melting using a mixture of elemental niobium and titanium powders. . *Mech. Work. Technol.* **2020**, *282*, 116646. [CrossRef]

39. Terrazas, C.A.; Murr, L.E.; Bermudez, D.; Arrieta, E.; Roberson, D.A.; Wicker, R.B. Microstructure and mechanical properties of Ti-6Al-4V-5% hydroxyapatite composite fabricated using electron beam powder bed fusion. *J. Mater. Sci. Technol.* **2018**, *35*, 309–321. [CrossRef]
40. Lesko, C.; Walker, J.; Middendorf, J.; Gockel, J. Functionally Graded Titanium–Tantalum in the Horizontal Direction Using Laser Powder Bed Fusion Additive Manufacturing. *JOM* **2021**, *73*, 2878–2884. [CrossRef]
41. Anstaett, C.; Seidel, D.-I.C.; Reinhart, D.-I.G. Fabrication of 3D Multi-material Parts Using Laser-based Powder Bed Fusion.
42. Sing, S.; Huang, S.; Goh, G.; Tey, C.; Tan, J.; Yeong, W. Emerging metallic systems for additive manufacturing: In-situ alloying and multi-metal processing in laser powder bed fusion. *Prog. Mater. Sci.* **2021**, *119*, 100795. [CrossRef]
43. Wen, Y.; Zhang, B.; Narayan, R.L.; Wang, P.; Song, X.; Zhao, H.; Ramamurty, U.; Qu, X. Laser powder bed fusion of compositionally graded CoCrMo-Inconel 718. *Addit. Manuf.* **2021**, *40*, 101926. [CrossRef]
44. Aerosint, D.M.C. Unlocking Multi-Material Additive Manufacturing. 2023.
45. Scaramuccia, M.G.; Demir, A.G.; Caprio, L.; Tassa, O.; Previtali, B. Development of processing strategies for multigraded selective laser melting of Ti6Al4V and IN718. *Powder Technol.* **2020**, *367*, 376–389. [CrossRef]
46. Yusuf, S.M.; Mazlan, N.; Musa, N.H.; Zhao, X.; Chen, Y.; Yang, S.; Nordin, N.A.; Mazlan, S.A.; Gao, N. Microstructures and Hardening Mechanisms of a 316L Stainless Steel/Inconel 718 Interface Additively Manufactured by Multi-Material Selective Laser Melting. *Metals* **2023**, *13*, 400. [CrossRef]
47. Liu, Z.H.; Zhang, D.Q.; Sing, S.L.; Chua, C.K.; Loh, L.E. Interfacial characterization of SLM parts in multi-material processing: Metallurgical diffusion between 316L stainless steel and C18400 copper alloy. *Mater. Charact.* **2014**, *94*, 116–125. [CrossRef]
48. Nadimpalli, V.K.; Dahmen, T.; Valente, E.H.; Mohanty, S.; Pedersen, D.B. Multi-material additive manufacturing of steels using laser powder bed fusion. In *euspen's 19th International Conference & Exhibition*; The European Society for Precision Engineering and Nanotechnology: Bilbao, Spain, 2019; pp. 240–243. Available online: www.euspen.eu (accessed on 18 December 2024).
49. Zhou, J.; Li, H.; Yu, Y.; Li, Y.; Qian, Y.; Firouzian, K.; Lin, F. Fabrication of functionally graded materials from a single material by selective evaporation in electron beam powder bed fusion. *Mater. Sci. Eng. A* **2020**, *793*, 139827. [CrossRef]
50. Guo, C.; Ge, W.; Lin, F. Dual-Material Electron Beam Selective Melting: Hardware Development and Validation Studies. *Engineering* **2015**, *1*, 124–130. [CrossRef]
51. Fu, Z.; Ye, J.; Franke, M.; Körner, C. A novel approach for powder bed-based additive manufacturing of compositionally graded composites. *Addit. Manuf.* **2022**, *56*, 102916. [CrossRef]
52. Yuan, M.; Karamchedu, S.; Fan, Y.; Liu, L.; Nyborg, L.; Cao, Y. Study of defects in directed energy deposited Vanadis 4 Extra tool steel. *J. Manuf. Process.* **2022**, *76*, 419–427. [CrossRef]
53. Oliver, W.C.; Pharr, G.M. An improved technique for determining hardness and elastic modulus using load and displacement sensing indentation experiments. *J. Mater. Res.* **1992**, *7*, 1564–1583. [CrossRef]
54. Hinojos, A.; Mireles, J.; Reichardt, A.; Frigola, P.; Hosemann, P.; Murr, L.E.; Wicker, R.B. Joining of Inconel 718 and 316 Stainless Steel using electron beam melting additive manufacturing technology. *Mater. Des.* **2016**, *94*, 17–27. [CrossRef]
55. @Uddeholms AB. Uddeholm Vanadis®4 Extra SuperClean. October 2017. Available online: https://www.uddeholm.com/app/uploads/sites/216/productdb/api/tech_uddeholm-vanadis-4-extra_en.pdf (accessed on 18 December 2024).
56. Bean, C.; Wang, F.; Charpagne, M.; Villechaise, P.; Valle, V.; Agnew, S.; Gianola, D.; Pollock, T.; Stinville, J. Heterogeneous slip localization in an additively manufactured 316L stainless steel. *Int. J. Plast.* **2022**, *159*, 103436. [CrossRef]